



**HAL**  
open science

# Adiabatic shear banding induced degradation in a thermo-elastic/viscoplastic material under dynamic loading

Patrice Longère, André Dragon, Hervé Trumel, Xavier Deprince

► **To cite this version:**

Patrice Longère, André Dragon, Hervé Trumel, Xavier Deprince. Adiabatic shear banding induced degradation in a thermo-elastic/viscoplastic material under dynamic loading. *International Journal of Impact Engineering*, 2005, 32, pp.285-320. 10.1016/j.ijimpeng.2005.03.002 . hal-00443816

**HAL Id: hal-00443816**

**<https://hal.science/hal-00443816>**

Submitted on 4 Feb 2022

**HAL** is a multi-disciplinary open access archive for the deposit and dissemination of scientific research documents, whether they are published or not. The documents may come from teaching and research institutions in France or abroad, or from public or private research centers.

L'archive ouverte pluridisciplinaire **HAL**, est destinée au dépôt et à la diffusion de documents scientifiques de niveau recherche, publiés ou non, émanant des établissements d'enseignement et de recherche français ou étrangers, des laboratoires publics ou privés.



Distributed under a Creative Commons Attribution - NonCommercial 4.0 International License

# Adiabatic shear banding-induced degradation in a thermo-elastic/viscoplastic material under dynamic loading

Patrice Longère<sup>a,\*</sup>, André Dragon<sup>b,1</sup>, Hervé Trumel<sup>c</sup>, Xavier Deprince<sup>d</sup>

<sup>a</sup>*Laboratoire de Génie Mécanique et Matériaux, Université de Bretagne Sud, Rue de Saint-Maudé, BP 92116, 56321 Lorient Cedex, France*

<sup>b</sup>*Laboratoire de Mécanique et de Physique des Matériaux, UMR CNRS n°6617, ENSMA -1 avenue C. Ader, BP 40109, 86961 Futuroscope-Chasseneuil Cedex, France*

<sup>c</sup>*Commissariat à l'Energie Atomique, Direction des Applications Militaires, Le Ripault, BP16, 37260 MONTS, France*

<sup>d</sup>*GIATIndustries, 7 route de Guerry, 18023 Bourges Cedex, France*

In the approach presented, adiabatic shear banding (ASB) is considered as a form of anisotropic deterioration. The anisotropic mechanical degradation induced in the structural material by the bands is dealt with by using a second-order tensor internal variable. The kinematical consequences of the presence of the bands are described by means of the corresponding part (deterioration-induced part in addition to the genuinely plastic part) of the velocity gradient embodying the notion of a “super-dislocation”. The kinematical framework involves finite strain anisotropic elastic-irreversible formulation based on the multiplicative decomposition of the deformation gradient. Constitutive equations integrating ASB-deterioration-like process are derived from thermodynamic potentials namely the free energy and dissipative potentials in the general framework of the internal state variables formulation. The hypothesis of a single yield function has been put to describe the chronology of the viscoplastic dissipative mechanisms and to account for the strong coupling between plasticity and band induced deterioration. An auxiliary indicator needed for determining the conditions for shear bands initiation and orientation has been obtained from a simplified analysis based on the linear theory of perturbations. This three-dimensional

---

\*Corresponding author.

*E-mail addresses:* patrice.longere@univ-ubs.fr (P. Longère), dragon@lmpm.ensma.fr (A. Dragon).

<sup>1</sup>Also Correspondence to.

constitutive model, including anisotropic effects due to the ASB-induced deterioration in the context of finite elastic–plastic strains, rate sensitivity, strain hardening and thermal softening, has been implemented as ‘user material’ in the finite element code LS-DYNA. Three-dimensional numerical simulations of adiabatic shear banding-induced degradation have been performed considering the hat shape structure under dynamic shearing employing a direct Hopkinson pressure bar device. Depending on the impact velocity and on the loading duration, deterioration bands propagate or arrest inside the hat shape structure. Numerical results show the evolution of the band tip velocity during the deterioration process. Numerical deterioration maps inside the hat shape structure and the load transmitted to the output bar are in good agreement with experimental evidence including band orientation. Because of the modelling scale we use herein, mesh refining in the areas crossed by the bands—which usually supposes the a priori knowledge of the band trajectory—is not necessary. Thanks to the regularising effects of viscosity (in the model viscosity is double, concerning plasticity but also deterioration) and a further adaptive time procedure, a weak mesh dependency of the numerical results has been observed.

*Keywords:* Adiabatic shear banding; Anisotropic finite strain; Non-linear mechanics; Viscoplasticity; Finite element

## 1. Introduction and scope

Adiabatic shear banding (ASB) is recognised as a phenomenon of notable importance, as a failure precursor, in the field of dynamic deformation for a large class of metals and alloys (in particular high-strength steels and alloys). Stemming from the pioneering work of Zener and Hollomon [1], Recht [2], extensive investigation (metallurgical and mechanical, experimental and theoretical) and relevant literature have been devoted to the matter, see for instance numerous references given by Bai and Dodd [3] and more recently by Wright [4]. These authors have attempted complementary syntheses of the field ranging from material science-oriented research to non-linear mechanics issues. The special issue of *Mechanics of Materials* published in 1994, on *Shear Instabilities and Viscoplasticity Theories*, keeps also its topical importance. As pointed by Woodward [5], adiabatic shear mode requiring that thermal conductivity effects be attenuated by a small deformation time (high strain rates), it is therefore frequently “a characteristics of impact loading” (cf. [5, p.79]).

Depending on the thermo-mechanical properties of the target material and on the intensity of loading, the penetration of a flat end projectile into a hard steel plate can be accompanied by the formation of a ring shape intense (localised) shear zone inside the target. The intense shearing can lead to the development of adiabatic shear bands which are known as precursor of the ultimate dynamic plugging of the plate. In the present authors opinion accurate prediction of the protection response during the target/penetrator interaction needs an advanced three-dimensional (3D) description of the behaviour of the structural material containing adiabatic shear bands. The 3D TEVPVD (for Thermo Elastic ViscoPlastic with Viscous Deterioration) constitutive model and the inherent numerical formalism presented in this paper aim to describe the post-critical behaviour of a high-strength material in the presence of adiabatic shear bands evolution.

In the present approach, ASB is considered as a specific anisotropic deterioration process. Some earlier tentatives in this direction are due to Pecherski and Perzyna and coworkers, see e.g. [6,7]. The constitutive model to be formulated is intended to describe the thermo-elastic/viscoplastic

behaviour of the sound material and the mechanical anisotropy (directional degradation of both elastic and viscoplastic moduli) induced by ASB in the framework of large anisotropic elastic–plastic deformation.

### 1.1. Kinematical preliminaries

Let  $C_0$  be the initial undeformed configuration of the material, and  $C_t$  its deformed configuration at current time  $t$ . In order to account for finite inelastic strain, the pseudo-intermediate configuration  $C_{\text{inter}}$  is introduced by local elastic unloading with respect to the current configuration  $C_t$ . Suppose now that a form of permanent anisotropy is induced during inelastic deformation. It seems thus natural to define this anisotropy in the intermediate configuration  $C_{\text{inter}}$  which becomes henceforth a pseudo-material configuration (see e.g. [8]). To freeze anisotropy axes in the intermediate configuration  $C_{\text{inter}}$ , one applies a virtual unloading consisting in a purely elastic stretching  $\mathbf{V}^e$  and a rotation  $\mathbf{Q}^{-1}$  (following the works [9,10]). This leads to the decomposition of the deformation gradient  $\mathbf{F}$  as the product  $\mathbf{F} = \mathbf{V}^e \mathbf{Q} \mathbf{F}^{\text{in}}$ , as shown in Fig. 1, where  $\mathbf{F}^{\text{in}}$  represents the inelastic deformation.

Consider anisotropy directional effects represented by the unit vector  $\mathbf{n}$  and the second-order tensor  $\mathbf{N} = \mathbf{n} \otimes \mathbf{n}$  expressed in the intermediate configuration  $C_{\text{inter}}$  with respect to the laboratory fixed frame. Through the orthogonal rotation  $\mathbf{Q}$ , the structure tensors  $\mathbf{n}$  and  $\mathbf{N}$  are, respectively, transformed into  $\tilde{\mathbf{n}} = \mathbf{Q}\mathbf{n}$  and  $\tilde{\mathbf{N}} = \mathbf{Q}\mathbf{N}\mathbf{Q}^T$ . Their objective rates  $\overset{\nabla}{\tilde{\mathbf{n}}} = \mathbf{Q}\dot{\mathbf{n}}$  and  $\overset{\nabla}{\tilde{\mathbf{N}}} = \mathbf{Q}\dot{\mathbf{N}}\mathbf{Q}^T$  are thus expressed by  $\overset{\nabla}{\tilde{\mathbf{n}}} = \dot{\tilde{\mathbf{n}}} - \mathbf{W}\tilde{\mathbf{n}}$  and  $\overset{\nabla}{\tilde{\mathbf{N}}} = \dot{\tilde{\mathbf{N}}} - \mathbf{W}\tilde{\mathbf{N}} + \tilde{\mathbf{N}}\mathbf{W}$ , with the rotation rate  $\mathbf{W}$  being given by  $\mathbf{W} = \dot{\mathbf{Q}}\mathbf{Q}^T$ .

### 1.2. Physical motivations

With respect to the thermo-elastic/viscoplastic deformation of the ‘sound’ material, adiabatic shear bands generate locally discontinuities not only in the velocity gradient but also in the temperature field (see Fig. 2). In the presence of ASB coexist two different deformation patterns inside the medium : a ‘regular’ one relative to the material outside the bands, and a ‘singular’ one

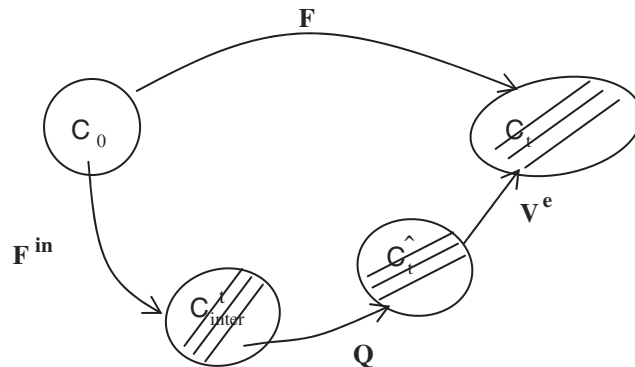


Fig. 1. Intermediate configuration as pseudo material configuration.

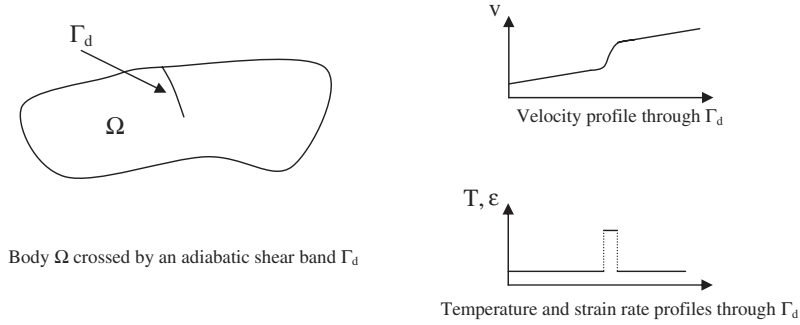


Fig. 2. ASB-induced discontinuities.

relative to the material inside the bands. Let suppose that the evolution of ‘regular’ and ‘singular’ processes can be described via the evolution of state variables such like relevant measures of elastic strain  $\mathbf{e}^e$ , temperature  $T$ , strain hardening  $p$ , damage  $\delta$ , metallurgical state  $\xi$ , and so on:

$$V_{\text{regular}} = (\mathbf{e}^e, T, p, \delta, \xi, \dots) \quad \text{and} \quad V_{\text{singular}} = (\mathbf{e}^{e*}, T^*, p^*, \delta^*, \xi^*, \dots),$$

where  $V_{\text{regular}}$  and  $V_{\text{singular}}$  represent, respectively, the sets of ‘regular’ and ‘singular’ state variables.

At an advanced stage of deformation, ‘singular’ elastic strain can be neglected, while a specific ‘singular’ variable describing intense shearing will be introduced further. We then have tentatively

$$V_{\text{regular}} = (\mathbf{e}^e, T, p, \delta, \xi, \dots) \quad \text{and} \quad V_{\text{singular}} = (T^*, p^*, \delta^*, \xi^*, \dots).$$

Before the ASB onset, solely ‘regular’ processes run:

$$V_{\text{regular}} = (\mathbf{e}^e, T, p, \delta, \xi, \dots) \quad \text{and} \quad V_{\text{singular}} = (0, 0, 0, 0, \dots).$$

After the ASB onset, evolutions of ‘regular’ and ‘singular’ processes, associated to representative volume element (RVE) whose length scale  $g$  is lower than the band width  $l$ , i.e.  $g < l$ , and which are, respectively, located outside and inside the band, become significantly distinct:

$$V_{\text{regular}} = (\mathbf{e}^e, T, p, \delta, \xi, \dots) \quad \text{and} \quad V_{\text{singular}} = (T^*, p^*, \delta^*, \xi^*, \dots).$$

This is shown in the following figure (Fig. 3).

Thus, the maximal value of the ‘regular’ strain measured in any RVE located outside the band can be less than 3 while the value of the ‘singular’ strain measured in any RVE located inside the band can be greater than 15. This is due to localisation phenomena under consideration. In the same way, the maximal value of the ‘regular’ temperature measured in any small RVE located inside the structure (except the band) is generally less than 500 K while the value of the ‘singular’ temperature measured in any RVE located inside the band can be greater than 1500 K.

These remarks can be extended to the other state variables.

The choice of a ‘small’ RVE, whose length scale is lower than the band width ( $g < l$ ), is not what is subsequently followed in our modelling. The more global insight is preferred (‘large’ RVE whose length scale is greater than the band width, i.e.  $g > l$ ) with all the set of ‘singular’ variables (and respective dissipation effects), and notably the ‘singular’ temperature  $T^*$ , being incorporated in an adequate deterioration (internal) variable.

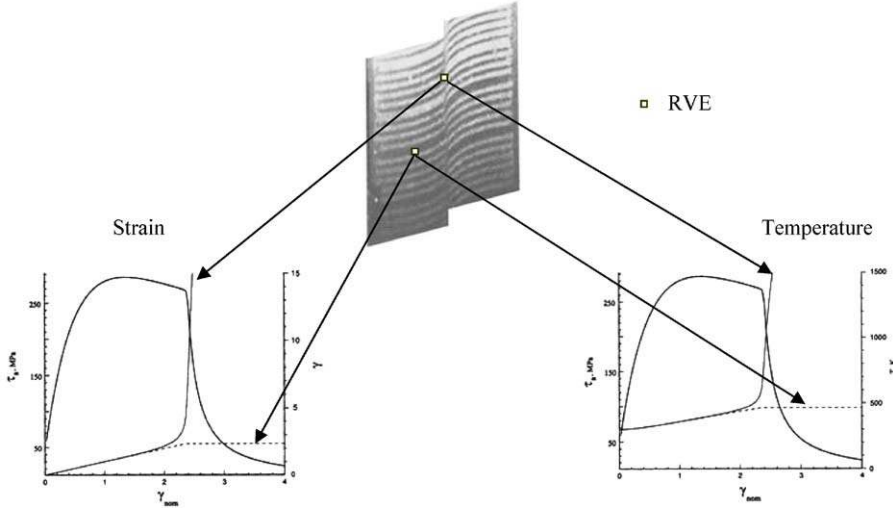


Fig. 3. ‘Regular’ and ‘singular’ variables evolution analysis. Curves are extracted from [11].

A fine description of the processes intervening in the band supposes obviously a micromechanical approach. Our approach is actually an alternative to such a description, which is of course a valuable one but which cannot be easily applied for ‘larger scale’ structure shock response analysis involving ASB effects. The latter is the context of the modelling proposed.

We do consider actually a RVE whose length scale is greater than the bandwidth ( $g > \lambda$ ). We do not use genuine micro–macro transition (homogenisation) but a phenomenological approach accounting for physical features concerning in particular ASB formation and development. The consequences of the presence of bands at the RVE scale we use ( $g > \lambda$ ) are three:

- mechanical softening;
- structural anisotropy;
- additional kinematics.

In our approach, the evolution of the ‘singular’ dissipative processes (intervening inside the band) contributing to this macromechanical softening is described via the evolution of a single internal variable called  $d^\alpha$ ,  $\alpha$  designating a family of bands with the same orientation. The softening of the RVE behaviour being considered as a form of mechanical degradation, the variable  $d^\alpha$  must then be able to describe the deterioration state of the RVE induced by the presence of the bands (ASB related feedback deterioration). It characterises the global material deterioration under ASB as shown in the following figure (Fig. 4).

The variable  $d^\alpha$  is then a function of the ‘singular’ state variables and of the characteristic length  $\lambda^\alpha$  of the band:

$$d^\alpha = d^\alpha(\lambda, V_{\text{singular}}) = d^\alpha(\lambda, T^*, p^*, \delta^*, \xi^*, \dots).$$

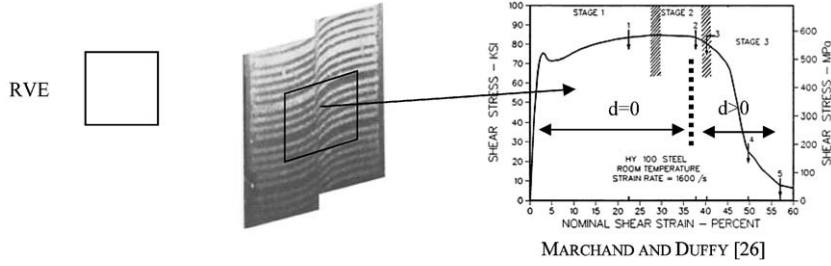


Fig. 4. ‘Large RVE’ concept illustrated by Marchand and Duffy dynamic torsion experiments ( $\alpha = 1$ ).

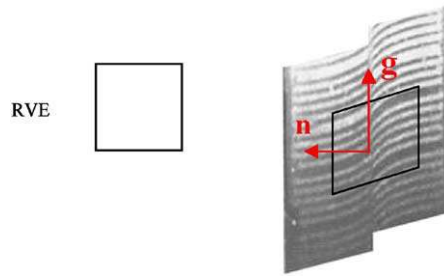


Fig. 5. Orientation tensor  $\mathbf{N} = \mathbf{n} \otimes \mathbf{n}$  ( $\alpha = 1$ ).

A micromechanical analysis followed by any averaging procedure could have lead to an explicit form for  $d^\alpha$ . This is not the purpose of our work as it is hardly feasible actually regarding strongly non-linear phenomena involved and high strain rate context. What we are putting forward is a phenomenological description involving ‘singular’ dissipative evolution due to ASB entirely incorporated in the evolution of  $d^\alpha$ . In our phenomenological approach, evolution law of  $d^\alpha$  is given by the normality rule under the assumption of the existence of a respective dissipative potential.

In such a description, an increase of the ‘singular’ temperature  $T^*$  (the temperature inside the band) provokes an increase of the magnitude of  $d^\alpha$  without causing an explicit increase of the ‘regular’ temperature  $T$  (the temperature outside the band), preserving the hypothesis of local adiabaticity.

Considering a single band system ( $\alpha = 1$ ), the lower bound  $d_{\min} = d(T_{\text{onset}}, \dots)$  of the density  $d$  is obviously zero,  $T_{\text{onset}}$  representing the initial ‘singular’ temperature value which is equal to the ‘regular’ temperature value at the incipience of ASB. On the other hand, temperature is supposed to be bounded in the band material by the melting point. This is probably a strongly over-estimating statement for metallic materials concerned by this mechanism of ASB. The magnitude of  $d$  is consequently bounded too. The upper bound of  $d$  is denoted as  $d_{\max} = d(T_m, \dots)$ , where  $T_m$  represents the temperature value at the melting point.

In the same way, the structural anisotropy induced in the RVE ( $g > \lambda$ ) by the presence of the bands is linked to the orientation  $\mathbf{n}^\alpha$  of the band, through the orientation tensor  $\mathbf{N}^\alpha = \mathbf{n}^\alpha \otimes \mathbf{n}^\alpha$ , as shown in Fig. 5.

The combination of  $d^\alpha$  and  $\mathbf{n}^\alpha$  allows for describing entirely the specific orthotropic mechanical degradation of the RVE under ASB. This combination is performed in the present approach through the definition of a second-order tensorial variable as follows:

$$\mathbf{D} = \sum_{\alpha} d^{\alpha} \mathbf{N}^{\alpha}, \quad (1)$$

where

$$\begin{aligned} d^{\alpha} &= d^{\alpha}(\lambda, T^*, p^*, \delta^*, \xi^*, \dots), \\ \mathbf{N}^{\alpha} &= \mathbf{n}^{\alpha} \otimes \mathbf{n}^{\alpha}. \end{aligned} \quad (2)$$

With this definition, the current density  $d$  of the deterioration tensor  $\mathbf{D}$  depends notably on the ‘singular’ temperature  $T^*$ , i.e.  $d = d(T^*, \dots)$ , the dots signifying other arguments, see also [13,14]. As  $\mathbf{D}$  quantifies adiabatic shear band-induced degradation of the RVE, this variable can be considered as a sort of ‘degradation’ variable.

In the model presented, involving ‘large’ RVE reference scale, the set of state variables is thus reduced to:

$$V = (\mathbf{e}^e, T, p; \mathbf{D}).$$

The approach is summarised in Table 1.

While  $\mathbf{D}$  governs the anisotropic degradation, kinematical consequences of the presence of the bands, viewed as those of an idealised ‘super-dislocation’ (by analogy, respective scales being obviously different) within the representative volume (Fig. 4), are dealt with by incorporating the resulting contribution  $\mathbf{L}^d \propto \sum_{\alpha} \dot{\gamma}^{\alpha} \mathbf{g}^{\alpha} \otimes \mathbf{n}^{\alpha}$  in the macroscopic description of the deformation (see also [6]), where  $\alpha$  represents the system of bands,  $\dot{\gamma}^{\alpha}$  the band related glide velocity,  $\mathbf{n}^{\alpha}$  the normal to the band and  $\mathbf{g}^{\alpha}$  the glide direction. There are thus two contributions to the inelastic velocity gradient  $\mathbf{L}^{dp}$ :  $\mathbf{L}^p$  relative to homogeneous ‘regular’ viscoplasticity, and  $\mathbf{L}^d$ , as mentioned above, resulting from ASB-induced ‘singular’ mechanism, such as  $\mathbf{L}^{dp} = \mathbf{L}^p + \mathbf{L}^d$ .

Notice that the kinematic variable  $\mathbf{d}^d$  allows to smooth the boundary discontinuity caused by the ASB, as shown in the following figure (Fig. 6).

Table 1  
Definition of the ‘large RVE’ state variables set from ‘regular’ and ‘singular’ state variables sets

Approach	RVE length scale	State variables
Fine scale (micro and meso scale)	$g < \lambda$	$V_{\text{regular}} = (\mathbf{e}^e, T, p, \delta, \xi, \dots)$ and $V_{\text{singular}} = (T^*, p^*, \delta^*, \xi^*, \dots)$ $(T^*, p^*, \delta^*, \xi^*, \dots) \oplus (\lambda, \eta)$ $d \oplus \mathbf{n}$ $\mathbf{D} = d \mathbf{n} \otimes \mathbf{n}$
Present	$g > \lambda$	$V = (\mathbf{e}^e, T, p, \delta, \xi, \dots, \mathbf{D})$

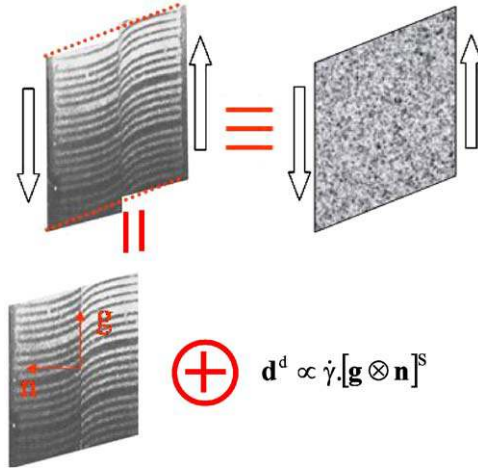


Fig. 6. ‘Super dislocation’ concept applied to ASB kinematics.

In relation with the previous subsection, the band-induced anisotropy is defined in the intermediate configuration  $C_{\text{inter}}$  associated with the multiplicative decomposition of the deformation gradient  $\mathbf{F}$  as the product  $\mathbf{F} = \mathbf{V}^e \mathbf{Q} \mathbf{F}^{\text{dp}}$  (see Fig. 1), where  $\mathbf{F}^{\text{dp}} = \mathbf{F}^{\text{in}}$ . Objectivity of the tensor variables, and notably of their derivatives, expressed in the current configuration is required for consistent constitutive modelling. Objectivity associated with anisotropy effects is not a trivial problem in the framework of finite deformation plasticity, see e.g. [15]. In accordance

with [10], we employ here a specific rotational derivative, namely  $\overset{\nabla}{\dot{\mathbf{A}}} = \dot{\mathbf{A}} - \mathbf{W}\mathbf{A} + \mathbf{A}\mathbf{W}$  for the rate of the second-order tensor  $\mathbf{A}$ , where  $\mathbf{W} = \dot{\mathbf{Q}}\mathbf{Q}^T$ . In this framework (anisotropy, finite inelastic deformation), the constitutive model should include the relationship for the inelastic spin in addition to the respective strain rate (see [16,17]). The former is furthermore indispensable to calculate the rotation rate  $\mathbf{W}$  occurring in the rotational derivatives. Under the assumption of small elastic deformations,  $\mathbf{W} = \boldsymbol{\omega} - \boldsymbol{\omega}^{\text{dp}}$  (see [13]), where  $\boldsymbol{\omega}$  represents the total spin (antisymmetric part of the velocity gradient  $\mathbf{L}$ ) and  $\boldsymbol{\omega}^{\text{dp}}$  the deterioration-plastic (inelastic) spin.

At the macroscopic level, the presence of the bands implies degradation of the elastic properties (inducing a form of elastic orthotropy due to tensorial character of  $\mathbf{D}$ ) together with a change in the direction of yielding (inducing distortion of the yield surface). In the general framework of irreversible thermodynamics, interference of the band-related yielding and the ‘regular’ plasticity is interpreted in terms of couplings, respectively, in the energy potential (free energy) and in the dissipative potentials.

The constitutive model to be detailed in Section 2 is finally completed by an auxiliary indicator of the ASB onset. Conditions for localisation are actually deduced from a simplified analysis based on the linear theory of perturbations. They are expressed as a criterion relating the maximum shear stress to parameters depending on the constitutive relations. This criterion, which provides the conditions for the adiabatic shearing initiation and the incipient band orientation, preserves 3D features of the process.

As mentioned above we detail in Section 2 the constitutive relations including finite anisotropic elastic–plastic strain, rate sensitivity, strain hardening, thermal softening and anisotropic

deterioration by ASB, together with the auxiliary indicator needed for activating the deterioration process.

In Section 3 we present some aspects relative to the numerical algorithmic formulation of the model and its implementation as user material in the finite element engineering code LS-DYNA. Numerical results concerning the hat shape structure (HSS) dynamic shearing, employing a direct Hopkinson pressure bar device, are discussed and compared with experiments in Section 4.

## 2. The 3D constitutive model

Following the heuristic methodology outlined above makes possible the macromechanical description of the post-critical behaviour of the material containing adiabatic shear bands within continuum theory framework, including the dissipative mechanisms of viscoplasticity and band-induced deterioration.

The modelling aims at describing the material behaviour not only during the first stage of locally homogeneous and weakly inhomogeneous (stages 1 and 2 as defined in [12]) deformation but also during the phase of strong localisation induced by the formation of ASB (stage 3 as defined in [12]). The model should thus be robust enough to overcome local instabilities relative to inception and growth of ASB on mesoscale level. Another feature to be accounted for by this model is a strongly oriented character of ASB thus inducing significant mechanical anisotropy with both elasticity and plasticity being potentially affected.

### 2.1. The constitutive model

Based on irreversible thermodynamics with internal variables, the constitutive model is detailed below to be applied later in the context of high-velocity impact and penetration mechanics. Some simplifying assumptions, regarding notably strain and strain rate hardening description and small elastic strain, have been made.

In the model presented, involving ‘large’ RVE reference scale  $g > \lambda$ , the set of state variables is

$$V = (\mathbf{e}^e, T, p; \tilde{\mathbf{D}}),$$

where  $\mathbf{e}^e$  represents a measure of the elastic deformation ( $\mathbf{e}^e = \frac{1}{2} \ln(\mathbf{b}^e) = \ln(\mathbf{V}^e)$ ;  $\mathbf{F}^e = \mathbf{V}^e \mathbf{R}^e$ ),  $T$  the absolute ‘regular’ temperature,  $p$  the scalar isotropic strain hardening variable, and  $\tilde{\mathbf{D}} = d\tilde{\mathbf{n}} \otimes \tilde{\mathbf{n}} = \mathbf{QDQ}^T$  the objective deterioration internal variable in current (actual) configuration  $C_t$ .

It is noteworthy that the set  $(\mathbf{e}^e, T, p)$  corresponds exactly to the ‘regular’ state variables mentioned above while  $\tilde{\mathbf{D}}$  describes globally the ‘singular’ effects at the actual ‘large’ RVE scale.

#### 2.1.1. Thermo-elastic response and strain hardening. ASB-related energy release rate

The thermo-elastic response of the anisotropic medium is supposed to be described via a thermodynamic potential, namely the specific free energy  $\psi(\mathbf{e}^e, T; p, \tilde{\mathbf{D}})$ . The free energy per unit initial volume is further additively decomposed into a reversible part  $\rho_0 \psi^e(\mathbf{e}^e, T; \tilde{\mathbf{D}})$ , namely the elastic term, and the stored energy term  $\rho_0 \psi^p(T; p, \tilde{\mathbf{D}})$ :

$$\rho_0 \psi(\mathbf{e}^e, T; p, \tilde{\mathbf{D}}) = \rho_0 \psi^e(\mathbf{e}^e, T; \tilde{\mathbf{D}}) + \rho_0 \psi^p(T; p, \tilde{\mathbf{D}}). \quad (3)$$

The reversible (recoverable) part of the free energy includes the initial isotropic linear thermo-elasticity of the sound material and deterioration-induced orthotropic elasticity in the degraded material. It is being built from the theory of isotropic scalar functions of several tensorial arguments (see [18]). The elastic degradation is described as being dependent on  $\tilde{\mathbf{D}}$ , thus comprising deterioration-induced orthotropy effects via two terms involving material constants  $a$  and  $b$  below, see also [14,19]. It is assumed that possible interactions between different band clusters are not explicitly taken into account. The recoverable energy is written in the form

$$\rho_0\psi^e = \frac{\lambda}{2} e_{ii}^e e_{jj}^e + \mu e_{ii}^e e_{ji}^e - \alpha K e_{ii}^e \Delta T - \frac{\rho_0 C}{2T_0} \Delta T^2 - a e_{kk}^e e_{ij}^e \tilde{\mathbf{D}}_{ji} - 2b e_{ij}^e e_{jk}^e \tilde{\mathbf{D}}_{ki} \quad (4)$$

with  $\Delta T = T - T_0$ ,  $K = \lambda + 2\mu/3$  where  $\lambda$  and  $\mu$  represent Lamé's coefficients,  $K$  the bulk modulus,  $\alpha$  the thermal expansion coefficient,  $\rho_0$  the initial density,  $C$  the heat capacity,  $a$  and  $b$  constants related to elastic energy degradation caused by ASB.

The form of the stored energy reflects the competition that takes place in the material between hardening and softening. Hardening is a consequence of the micromechanisms of 'regular' plasticity, while softening is due to heating on the one hand and to current ASB-related deterioration on the other one. During their evolution (formation and propagation), ASB modify the state of internal stresses. In this sense, one can assume that deterioration acts much like temperature to release stored energy; as stated before the tensor  $\mathbf{D}$  comprises the effect of 'singular' temperature  $T^*$ . These considerations justify the choice of a multiplicative decomposition of softening into 'regular' heating and ASB-deterioration respective contributions.

$$\rho_0\psi^p = R_\infty \left[ p + \frac{1}{k} \exp(-kp) \right] \exp(-\gamma T) \exp\left(-d_1 \tilde{\mathbf{D}}_{ii} - \frac{d_2}{2} \tilde{\mathbf{D}}_{ij} \tilde{\mathbf{D}}_{ji}\right), \quad (5)$$

where  $R_\infty$  represents the saturation stress,  $k$  the plastic hardening parameter linked to the initial hardening modulus,  $\gamma$  the thermal softening parameter,  $d_1$  and  $d_2$  the deterioration (ASB) related softening constants.

The model, to be consistent with irreversible thermodynamic framework, should satisfy the Clausius–Duhem dissipation inequality. From the mechanical viewpoint, the latter is written as

$$D_{\text{int}} = \tau_{ij} d_{ji} - \rho_0 (\dot{\psi} + s\dot{T}) \geq 0. \quad (6)$$

Gibbs relation and Clausius–Duhem inequality are written as (see [13] for further details):

$$\begin{aligned} \rho_0 \dot{\psi} &= -\rho_0 s \dot{T} + \tau_{ij} d_{ji}^e + r \dot{p} - \tilde{k}_{ij} \overset{\nabla}{\tilde{\mathbf{D}}}_{ji}, \\ D_{\text{int}} &= \tau_{ij} d_{ji}^{\text{dp}} - r \dot{p} + \tilde{k}_{ij} \overset{\nabla}{\tilde{\mathbf{D}}}_{ji} \geq 0. \end{aligned} \quad (7)$$

The thermo-elastic Kirchhoff stress tensor  $\boldsymbol{\tau}$ , the strain hardening driving force  $\mathbf{r}$  as well as the deterioration conjugate force  $\tilde{\mathbf{k}}$  are derived from the thermodynamic potential with respect to  $\mathbf{e}^e$ ,  $p$  and  $\tilde{\mathbf{D}}$ :

$$\tau_{ij} = \rho_0 \frac{\partial \psi}{\partial e_{ij}^e} = \lambda e_{kk}^e \delta_{ij} + 2\mu e_{ij}^e - \alpha K \Delta T \delta_{ij} - a (e_{mn}^e \tilde{\mathbf{D}}_{nm} \delta_{ij} + e_{kk}^e \tilde{\mathbf{D}}_{ij}) - 2b (e_{ik}^e \tilde{\mathbf{D}}_{kj} + \tilde{\mathbf{D}}_{ik} e_{kj}^e), \quad (8)$$

$$r = \rho_0 \frac{\partial \psi}{\partial p} = R_\infty [1 - \exp(-kp)] \exp(-\gamma T) \exp\left(-d_1 \tilde{D}_{kk} - \frac{d_2}{2} \tilde{D}_{kl} \tilde{D}_{lk}\right), \quad (9)$$

$$\begin{aligned} \tilde{k}_{ij} = \rho_0 \frac{\partial \psi}{\partial \tilde{D}_{ij}} = & ae_{kk}^e e_{ij}^e + 2be_{ik}^e e_{kj}^e + R_\infty \left[ p + \frac{1}{k} \exp(-kp) \right] \exp(-\gamma T) \\ & \times \exp\left(-d_1 \tilde{D}_{kk} - \frac{d_2}{2} \tilde{D}_{kl} \tilde{D}_{lk}\right) [d_1 \delta_{ij} + d_2 \tilde{D}_{ij}]. \end{aligned} \quad (10)$$

In the same way entropy can be expressed via derivation of energy with respect to  $T$ .

The form of the hardening conjugate force (9) describes strain hardening with saturation stress and thermal softening. For recall, the competition between strain hardening and thermal softening is at the origin of local instability, ASB occurring when thermal softening overcomes strain hardening. Hardening conjugate force increases during pure hardening but decreases with heating and deterioration effects superposed on hardening, describing the aforementioned competition.

The ASB-induced deterioration conjugate force  $\tilde{\mathbf{k}}(\mathbf{e}^e, T; p, \tilde{\mathbf{D}})$  is the energy release rate with respect to  $\tilde{\mathbf{D}}$ . It includes a contribution from the reversible part of the free energy, and another one from the stored energy. The corresponding terms represent, respectively, elastic and stored energy release rates induced by the formation and development (multiplication and propagation) of ASB in the material (RVE). It is noteworthy that both contributions to the degradation conjugate force exist before ASB inception. It is actually assumed that a finite supply of energy  $\tilde{k}_{\text{inc}}$  is necessary to activate the deterioration process. The latter value is explicitly determined for each loading case by the auxiliary analysis allowing for ASB induced deterioration onset estimation (see Section 2.2 below).

### 2.1.2. Regular vs. singular dissipation contributions

The dissipation in Eq. (6) can be decomposed into a ‘regular’ part directly linked to plasticity and a ‘singular’ part resulting from the contribution of irreversible processes involving bands:

$$D_{\text{int}} = D_{\text{reg}} + D_{\text{sing}}, \quad (11)$$

where

$$D_{\text{reg}} = \tau_{ij} d_{ji}^p - r\dot{p}, \quad (12)$$

$$D_{\text{sing}} = \tau_{ij} d_{ji}^d + \tilde{k}_{ij} \overset{\nabla}{\tilde{D}}_{ji}. \quad (13)$$

‘Regular’ heating  $\dot{T}$  caused by plasticity outside the bands is then estimated from the relation established under the conventional adiabaticity assumption using Eq. (12):

$$\rho_0 C \dot{T} = \tau_{ij} d_{ji}^p - r\dot{p}. \quad (14)$$

This relation can be compared with the common one based on the works in [20]:

$$\rho_0 C \dot{T} = \beta \tau_{ij} d_{ji}^p, \quad (15)$$

where  $\beta$  represents the inelastic heat fraction.

The effects of ‘singular’ heating  $\dot{T}^*$  localised inside the band cluster are included, by definition of the deterioration variable  $\tilde{\mathbf{D}}$  (see Eqs. (1) and (2)), in the scalar density  $d(T^*, \dots)$ , evolving with the ongoing deterioration. In a first approximation, one can write using Eq. (13):

$$\rho_0 C \dot{T}^* \propto D_{\text{sing}} = \tau_{ij} d_{ji}^d + \tilde{k}_{ij} \tilde{D}_{ji}^{\nabla}. \quad (16)$$

The temperature rise effects inside the ASB are indeed included in the ‘singular’ dissipation which is now represented by the product  $D_{\text{sing}} = \tilde{k}_{ij} \tilde{D}_{ji}^{\nabla}$  in Eq. (13). The other singular term  $D_{\text{sing}}^{\text{in}} = \tau_{ij} d_{ji}^d$  in Eq. (13) is due to the ASB contribution to the total inelastic strain.

During the process of ASB-induced degradation, the ‘regular’ part of dissipation decreases while the ‘singular’ part of dissipation increases. Thus, ‘regular’ temperature reaches progressively a saturation value while ‘singular’ temperature increases. In our approach ‘regular’ temperature is explicitly calculated, while ‘singular’ temperature should be deduced from the specific form of relationship (2)<sub>1</sub>. As stated in the foregoing the corresponding effects are implicitly contained in the actual intensity  $d$  of the deterioration variable  $\tilde{D}$  (see Eq. (2)).

### 2.1.3. Yield function

A single yield function that includes both plasticity and deterioration effects is assumed to describe the evolution of ‘regular’ and ‘singular’ variables. The following extended form of the plasticity and deterioration loading function  $F$  is postulated (see for e.g. [21,22] for general anisotropic plasticity framework):

$$F(\tau_{ij}, r, \tilde{k}_{ij}) = \hat{J}_2^s(\tau_{ij}, \tilde{k}_{ij}) - (R_0 + r), \quad (17)$$

$$\hat{J}_2^s(\tau_{ij}, \tilde{k}_{ij}) = \sqrt{\frac{3}{2} s_{ij} P_{ijkl}(\tilde{k}_{mn}) s_{kl}}, \quad (18)$$

where  $s$  represents the deviatoric part of the Kirchhoff stress tensor. The fourth-order tensor  $\mathbf{P}(\tilde{k})$  inducing anisotropy in the plastic flow is assumed in the form

$$P_{ijkl} = \frac{1}{2} (\delta_{ik} \delta_{jl} + \delta_{il} \delta_{jk}) + 2 \sum_{q=2}^N \eta_q (\tilde{k}_{nm}^+ \tilde{N}_{nm})^q \tilde{M}_{ij} \tilde{M}_{kl}. \quad (19)$$

In Eq. (19)  $\tilde{\mathbf{M}} = [\tilde{\mathbf{g}} \otimes \tilde{\mathbf{n}}]^S$  (see Fig. 6),  $\mathbf{S}$  standing for a symmetric part of  $\tilde{\mathbf{g}} \otimes \tilde{\mathbf{n}}$ , designates the ASB orientation tensor (ASB being viewed as a ‘super-dislocation’) namely

$$\tilde{M}_{ij} = [\tilde{g}_i \tilde{n}_j]^S = \frac{1}{2} (\tilde{g}_i \tilde{n}_j + \tilde{g}_j \tilde{n}_i). \quad (20)$$

The expression  $\text{Tr}(\tilde{\mathbf{k}}^+ \tilde{\mathbf{N}})$  represents the difference in deterioration conjugate force from its onset value corresponding to ASB incipience (constrained thermodynamic description, see [23]):

$$\tilde{k}_{ij}^+ \tilde{N}_{ji} = \langle \tilde{k}_{ij} \tilde{N}_{ji} - k_{\text{inc}} \rangle \quad (21)$$

the bracket  $\langle \cdot \rangle$  defining the ramp function. To determine  $k_{\text{inc}} = \text{Tr}(\tilde{\mathbf{k}} \tilde{\mathbf{N}})_{\text{inc}}$  an auxiliary analysis based on a perturbation method is conducted for a particular loading path (see Section 2.2 below).

The function  $R_0$  which represents the radius of the initial Von Mises cylinder (without hardening) in the stress space must account further for heating and ASB-induced softening. It is

expressed as follows:

$$R_0 = R_i \exp(-\gamma T) \exp\left(-d_1 \tilde{D}_{kk} - \frac{d_2}{2} \tilde{D}_{mn} \tilde{D}_{nm}\right), \quad (22)$$

where  $R_i$  represents an internal stress.

In the absence of deterioration, the yield function in Eq. (17) is reduced to Von Mises criterion.

#### 2.1.4. Evolution laws

Shear banding being intrinsically a viscoplastic singular process, it is natural to consider it as rate dependent. Consequently, the existence of two dissipative potentials which refer, respectively, to the ‘regular’ plasticity and to the ‘singular’ ASB deterioration is assumed. In parallel, one may distinguish three stages during the deformation progress: before the onset of localisation ‘regular’ plasticity is the only dissipative mechanism; just after the onset of localisation both mechanisms, namely ‘regular’ plasticity and ‘singular’ deterioration coexist; when localisation advances, ASB deterioration process becomes progressively the prevalent dissipative mechanism.

The viscoplastic and deterioration potentials are assumed to be of the Perzyna’s type (see [24]):

$$\phi_p^c = \frac{Y}{n+1} \left\langle \frac{F}{Y} \right\rangle^{n+1}, \quad (23)$$

$$\phi_d^c = \frac{Z}{m+1} \left\langle \frac{F}{Z} \right\rangle^{m+1}, \quad (24)$$

where  $Y$  and  $n$  represent viscous parameters relative to ‘regular’ plasticity,  $Z$  and  $m$  viscous parameters relative to ‘singular’ ASB deterioration.

Evolution laws are consequently derived via the normality rule from  $\phi_p^c$  for  $\mathbf{d}^{dp} = \mathbf{d}^p + \mathbf{d}^d$  and  $\dot{p}$ , and from  $\phi_d^c$  for  $\tilde{\mathbf{D}}^{\nabla}$ , respectively.

Notice that

$$d_{ij}^{dp} = d_{ij}^p + d_{ij}^d = \frac{\partial \phi_p^c}{\partial \tau_{ij}} = A^p \frac{\partial F}{\partial \tau_{ij}}, \quad (25)$$

$$-\dot{p} = \frac{\partial \phi_p^c}{\partial r} = A^p \frac{\partial F}{\partial r}, \quad (26)$$

$$\tilde{D}_{ij}^{\nabla} = \frac{\partial \phi_d^c}{\partial \tilde{k}_{ij}} = A^d \frac{\partial F}{\partial \tilde{k}_{ij}}, \quad (27)$$

One obtains

$$d_{ij}^p = \frac{3}{2} A^p \frac{s_{ij}}{\hat{J}_2^s}, \quad (28)$$

$$d_{ij}^d = 3A^p \frac{\sum_{q=2}^N \eta_q (\tilde{k}_{mn}^+ \tilde{N}_{nm})^q s_{kl} \tilde{M}_{kl}}{\hat{J}_2^s} \tilde{M}_{ij}, \quad (29)$$

$$\dot{p} = A^p, \quad (30)$$

$$\overset{\nabla}{\mathbf{D}}_{ij} = \frac{3}{2} A^d \frac{\sum_{q=2}^N q \cdot \eta_q (\tilde{k}_{mn}^+ \tilde{N}_{nm})^{q-1} (s_{kl} \tilde{M}_{kl})^2}{\tilde{J}_2^s} \tilde{N}_{ij}. \quad (31)$$

The corresponding multipliers governing viscoplasticity and viscous deterioration are expressed by

$$A^p = \left\langle \frac{\partial \phi_p^c}{\partial F} \right\rangle = \left\langle \frac{F}{Y} \right\rangle^n, \quad (32)$$

$$A^d = \left\langle \frac{\partial \phi_d^c}{\partial F} \right\rangle = \left\langle \frac{F}{Z} \right\rangle^m. \quad (33)$$

The evolution laws verify the collinearity of the ‘regular’ plastic strain rate  $\mathbf{d}^p$  with the deviatoric part  $\mathbf{s}$  of the stress tensor, the collinearity of the ‘singular’ ASB induced strain rate  $\mathbf{d}^d$  with the orientation tensor  $\tilde{\mathbf{M}} = [\tilde{\mathbf{g}} \otimes \tilde{\mathbf{n}}]^S$ , and finally the collinearity of the objective deterioration rate  $\overset{\nabla}{\mathbf{D}}$  with the orientation tensor  $\tilde{\mathbf{N}} = \tilde{\mathbf{n}} \otimes \tilde{\mathbf{n}}$  for conservative deterioration growth configuration considered here.

Assuming a weak contribution of the ‘regular’ plastic spin  $\omega^p$  with regards to the ‘singular’ deterioration induced spin  $\omega^d$  [13] leads to the following simplified expression for the rotation rate:

$$W_{ij} = \omega_{ij} - \omega_{ij}^d. \quad (34)$$

The deterioration induced spin  $\omega^d$  is deduced from (29) as follows, where  $\tilde{\mathbf{T}} = [\tilde{\mathbf{g}} \otimes \tilde{\mathbf{n}}]^{AS}$ , AS standing for an antisymmetric part of  $\tilde{\mathbf{g}} \otimes \tilde{\mathbf{n}}$ :

$$\omega_{ij}^d = 3A^p \frac{\sum_{q=2}^N \eta_q (\tilde{k}_{pq}^+ \tilde{N}_{qp})^q s_{kl} \tilde{M}_{kl}}{\tilde{J}_2^s} \tilde{T}_{ij}. \quad (35)$$

## 2.2. ASB onset indicator

The phenomenon of ASB is known to occur in particular in thermo/viscoplastic metals as the result of a thermal instability. Many studies have been devoted to the identification of conditions for shear band initiation, using mostly the linear theory of perturbation. Nevertheless, obtaining operational conditions by means of this method needs (in practice, in the analyses known in the literature, see e.g. [25,26]) some strong assumptions regarding notably the material behaviour (which is supposed to be viscoplastic with elasticity being frequently neglected), the loading path (1D simple shear), the adiabaticity hypothesis, and the interpretation of the instability onset as the localisation one. In this case, the linear theory of perturbations is able to provide analytical conditions for ‘shear band’ (thermal instability actually) initiation, and also further information on parameters related to the process, for e.g. the band spacing (see [27]).

The constitutive model presented above is now completed in this manner by a deterioration incipience criterion based on a simplified analysis of material instability (in fact localisation upper

bound) in order to determine  $k_{\text{inc}} = (\tilde{\mathbf{k}} : \tilde{\mathbf{N}})_{\text{inc}}$  in Eq. (21), which activates the ASB-related rates  $\mathbf{d}^{\text{d}}$  and  $\tilde{\mathbf{D}}$ . The relevant approach is not detailed here, the reader can consult Ref. [13]. The aim is to give access to salient mechanical factors conditioning band-induced deterioration incipience according to the model presented. Besides the value of  $k_{\text{inc}}$ , orientation of the incipient localisation is searched for. The simple shear analysis is generalised for 3D case, employing the concept of super dislocation outlined before. In such a way the resolved shear stress  $\tau_{\text{res}} = \text{Tr}(\mathbf{s}\tilde{\mathbf{M}})$  appears in criterion (36) obtained and cited below. Moreover, when generalising the simple shear analysis to 3D configuration, it is assumed that adiabatic shear bands develop along the planes of maximal shear stress. Initiation, orientation and propagation of bands are thus supposed to be controlled by the following condition:

$$G\left(\tau_{ij}, r, \dot{p}; \frac{\partial r}{\partial p}, \frac{\partial r}{\partial T}\right) = \sqrt{3}|\tau_{\text{res}}| - \left(r - \frac{1}{n}Y\dot{p}^{1/n} + \rho_0 C \left(\frac{\partial r}{\partial p} / \left(-\frac{\partial r}{\partial T}\right)\right)\right) > 0, \quad (36)$$

where  $\tau_{\text{res}}$  represents the resolved shear stress,  $r$  the isotropic hardening conjugate force,  $Y\dot{p}^{1/n}$  the strain rate-induced overstress,  $\partial r/\partial p$  the plastic hardening and  $\partial r/\partial T$  the thermal softening.

According to this present simplified analysis outlined, band induced deterioration process is assumed to run as soon as  $G = 0$ . The main features of the aforementioned criterion are:

- the use of thermodynamic model introduced above;
- the determination of the 3D orientation of the entity (ASB) at the origin of the instability;
- the delay in the ASB initiation—by neglecting in the analysis the contribution of  $\partial R_0/\partial T$  to thermal softening—allowing to approach the localisation onset as an upper bound with respect to genuine instability onset.

This condition must be interpreted as the auxiliary indicator for the deterioration process incipience leading notably to the determination of the deterioration conjugate force threshold  $k_{\text{inc}} = (\tilde{\mathbf{k}} : \tilde{\mathbf{N}})_{\text{inc}}$ . Some analogy can be seen with the critical energy release rate in fracture mechanics.

According to the present non-linear model, critical values of temperature or deformation at the occurrence of the process of ASB are not imposed through an arbitrary standard but intimately linked to loading history.

### 2.3. Identification of material constants

As stated above, the TEVPVD model aims to be applied for dynamic loadings including penetration and perforation mechanisms. Regarding boundary value problems involving ASB, anisotropic deterioration, and fracture, employment of conventional constitutive laws is rapidly limited. The 3D model presented here, built on thermodynamic bases, intends to capture the material behaviour in the first phases of local degradation, namely during the process of ASB. It is also set to reproduce a wide range of metallic material behaviour, including those usually described via e.g. Johnson and Cook and Zerilli and Armstrong's engineering models (see [28,29]).

### 2.3.1. Viscoplasticity related constants

We employ the experimental data interpreted in terms of the well-known simplified engineering model by Johnson and Cook, as a sort of logistic support and an intermediate stage to determine finally the viscoplasticity (plastic flow, strain hardening, thermal softening) related material constants in the present model.

The thermo/elastic-viscoplastic set of material constants (the TEVP part of the model) for the high-strength steel (30NiCrMo6-6 with appropriate thermo-mechanical treatment), further considered in this study, have been identified explicitly from the corresponding set of Johnson–Cook’s material constants. Remind that Johnson–Cook’s engineering constitutive law is expressed by:

$$J_2(\tau) - (A + Bp^n)(1 + c \ln \dot{p})(1 - \bar{T}^m) = 0, \quad (37)$$

$$J_2(\tau) = \sqrt{\frac{3}{2} s_{ij} s_{ji}}, \quad (38)$$

$$\dot{p} = \frac{\dot{p}}{\dot{p}_{\text{réf}}}, \quad (39)$$

$$\bar{T} = \frac{T - T_{\text{room}}}{T_F - T_{\text{room}}}. \quad (40)$$

Heating is evaluated from Eq. (15).

The set of 30NiCrMo6-6 constants for Johnson–Cook’s engineering model, assembled in the left column of Table 2, has been obtained by Gailly [30] from compression tests in the ranges

$$-50^\circ\text{C} < T < 400^\circ\text{C}; 1\text{s}^{-1} < \dot{p} < 3000\text{s}^{-1}; 1\% < p < 40\%.$$

Table 2  
Viscoplastic related material constants for 30NiCrMo6-6

Johnson–Cook’s model [30]	TEVPVD model
$\rho_0 = 7800 \text{ kg/m}^3$	$\rho_0 = 7800 \text{ kg/m}^3$
$C = 420 \text{ J/kg K}$	$C = 420 \text{ J/kg K}$
$E = 200\,000 \text{ MPa}$	$E = 200\,000 \text{ MPa}$
$\nu = 0.33$	$\nu = 0.33$
$A = 612 \text{ MPa}$	$\alpha = 1.e - 6 \text{ K}^{-1}$
$B = 846 \text{ MPa}$	$R_i = 920 \text{ MPa}$
$n = 0.146$	$R_\infty = 400 \text{ MPa}$
$c = 0.0148$	$k = 10$
$\dot{p}_{\text{réf}} = 1 \text{ s}^{-1}$	$\gamma = 1.1e - 3 \text{ }^\circ\text{C}^{-1}$
$T_{\text{réf}} = 300 \text{ K}$	$Y = 60 \text{ MPa s}^{1/n}$
$T_F = 1793 \text{ K}$	$n = 6$
$m = 1.058$	
$\beta = 1$	

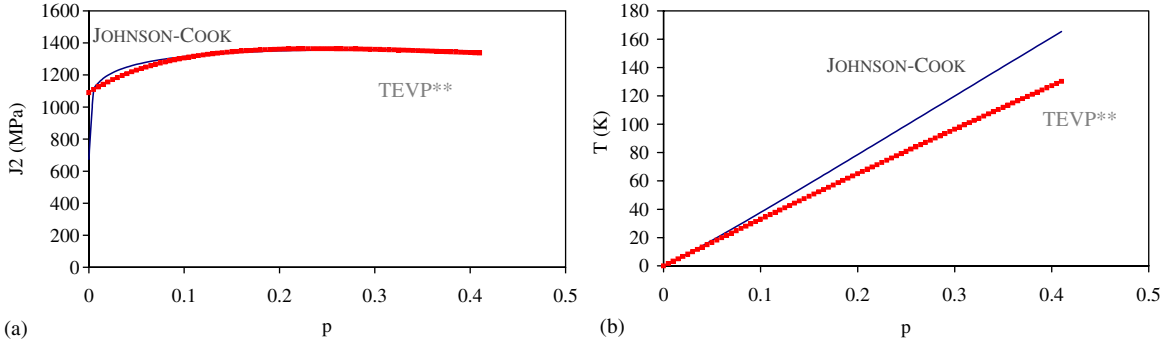


Fig. 7. Comparison of stress and temperature evolutions with respect to plastic strain using Johnson–Cook and TEVPVD models. 30NiCrMo6-6- $T_0 = 20^\circ\text{C} - \dot{p} = 10^{+3}\text{s}^{-1}$ : (a) Stress vs. plastic strain curves; (b) Heating vs. plastic strain curves.

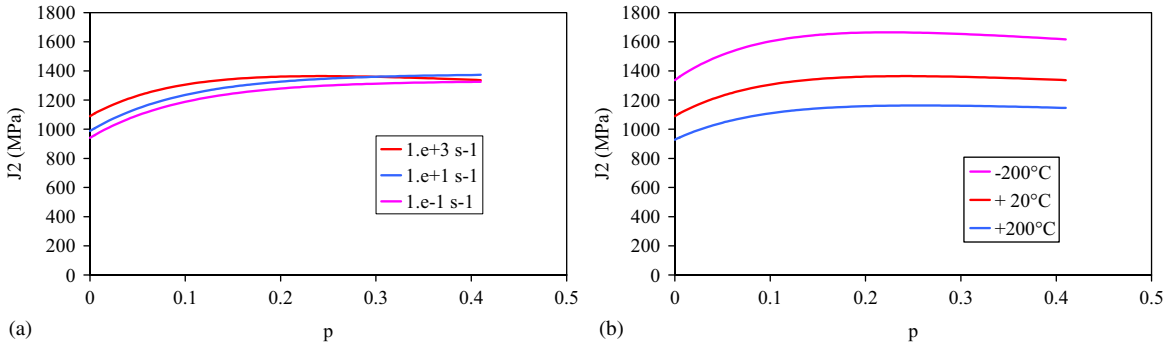


Fig. 8. Influences of plastic strain rate and temperature on the material behaviour using the TEVPVD model—30NiCrMo6-6; (a) Influence of plastic strain rate— $T_0 = 20^\circ\text{C}$ ; (b) influence of temperature— $\dot{p} = 10^{+3}\text{s}^{-1}$ .

The corresponding set of 30NiCrMo6-6 constants for the TEVPVD model including additional effects (as for e.g. saturation stress) giving more realistic representation has been reported in the right column of Table 2.

Fig. 7a and b are given in order to illustrate the feasibility of the identification of TEVPVD model constants from intermediate Johnson–Cook model constants. The discrepancy between heating evaluations (Fig. 7b) is dependent on the chosen value of the Taylor–Quinney coefficient (inelastic heat fraction in Eq. (15)).

Plastic response of the material considering the TEVPVD model is drawn for different strain rates and different initial temperatures in Fig. 8a and b. Adiabaticity hypothesis is supposed to be valid for strain rates up to  $10^{+2}\text{s}^{-1}$ .

### 2.3.2. Deterioration related constants of the TEVPVD model

In order to complete the description of the post-localisation behaviour of the material containing adiabatic shear bands, constants relative to band-induced deterioration in the actual

model have been further identified from Marchand and Duffy experimental results (see [16])—no data are actually available concerning the material at stake. Even if the material is slightly different, this simplification allows for giving a good idea of the model robustness in the post-localisation stage.

This identification leads to the deterioration related constants assembled in Table 3.

The reference curve shown in Fig. 9 has been obtained considering the simple shear of a volume element at a strain rate  $\dot{\Gamma}$  nominal value of  $1600 \text{ s}^{-1}$ . We insist once more on the fact that ASB-related deterioration is a direct consequence of the 3D material dissipative evolution together with the loading conditions via the simplified analysis summarised in the previous section—in other words, there is no need to impose an arbitrary phenomenological threshold to activate the deterioration process. In the present case, the critical shear strain value is close to 60% while the shear strain value at the maximum of the shear stress–shear strain curve is close to 40%. As observed experimentally (see [12]) and shown analytically (see [31]), localisation onset is actually not concomitant to instability incipience.

As drawn in Fig. 9, the three stages of deformation pointed in [12] are well reproduced (see also Fig. 4).

Table 3  
Deterioration related material constants for 30NiCrMo6-6

---

TEVPVD model

---

$$a = 0 \text{ MPa}$$

$$b = 15\,000 \text{ MPa}$$

$$d_1 = 0.05$$

$$d_2 = 0.05$$

$$N = 2$$

$$\eta_2 = 0.12 \text{ MPa}^{-2}$$

$$Z = 19 \text{ MPa s}^{1/m}$$

$$m = 2$$


---

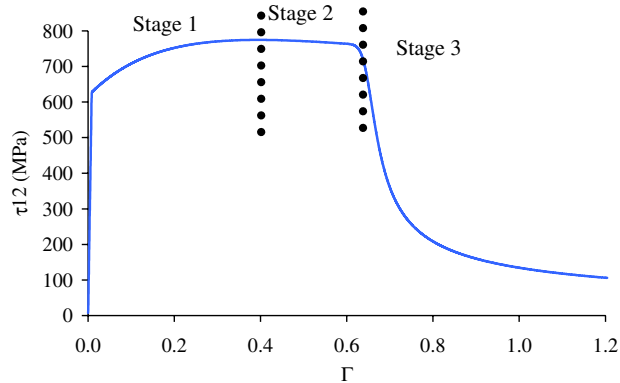


Fig. 9. Reference response (simple shear): 30NiCrMo6-6 -  $T_0 = 20^\circ\text{C}$  -  $\dot{\Gamma} = 1,6 \times 10^{+3} \text{ s}^{-1}$  -  $\Gamma = \dot{\Gamma}t$ .

### 3. Numerical simulations

The 3D TEVPVD constitutive model detailed in the previous section has been implemented as user material in the finite element code LS-DYNA and its numerical version has been evaluated considering the boundary value problem for the HSS subjected to dynamic shearing.

Integration of constitutive equations in the case of softening behaviour is not trivial, and there is no standard procedure. It is well known that viscosity contributes to regularise the boundary value problem but in the present case (strong localisation induced by ASB formation) a complementary procedure is needed to overcome numerical locking. This procedure allows for reducing locally (for the element concerned and not for the whole structure) the integration time step in order to ensure numerical convergence and stability.

*Numerical integration of the equations of motion:* Finite element simulation of a dynamic boundary value problem consists in solving the following generalised differential equations of motion which express the weak form of the momentum balance:

$$[M]\{\ddot{U}\} = \{F\} - \{I\}, \quad (41)$$

where  $[M]$  represents the (lumped) mass matrix,  $\{U\}$  the nodal displacement vector,  $\{F\}$  the external force vector, and  $\{I\}$  the internal force vector; the dots designate derivative with respect to time.

System (41) is integrated by the code LS-DYNA using the explicit method of centered finite difference. The value of a time step for the numerical integration is calculated with respect to Courant–Friedrichs–Lewy [32] condition for wave propagation:

$$\Delta t = \min_{\text{element}} \left( \frac{V}{C_k A} \right), \quad (42)$$

$$C_k = \sqrt{\frac{E(1-\nu)}{\rho(1+\nu)(1-2\nu)}}, \quad (43)$$

where  $\Delta t$  represents the time increment,  $V$  and  $A$  the volume and the area of the brick, and  $C_k$  the elastic wave celerity.

Because of the adiabaticity hypothesis, the simulation code does not consider the energy balance (in the sense of the thermal transfers).

*Numerical integration of the constitutive equations:* The non-linear constitutive model summarised here and implemented as ‘user material’ is governed by a system of differential equations which can be written as (see also [33]):

$$\dot{F} = A(F, t)F + f(F, t) \quad (44)$$

$$F = F(v, \rho, \tau, r, \tilde{\mathbf{k}}, \tilde{\mathbf{D}}, T), \quad (45)$$

where  $A(F, t)$  represents a linear differential operator, and  $f(F, t)$  a non-linear function.

The forward finite difference method has been used to integrate the above equations. In the framework of the present study, numerical stability and convergence are furthermore controlled by an adaptive time sub-increment procedure based on the maximum strain increment  $\Delta \bar{\epsilon}$

principle (see [34]):

$$\overline{\Delta t} = \frac{\Delta \bar{\epsilon}}{\dot{\bar{\epsilon}}}, \quad (46)$$

$$\dot{\bar{\epsilon}} = \sqrt{\frac{2}{3} d_{ij} d_{ji}}, \quad (47)$$

where  $\overline{\Delta t}$  represents the adaptive time sub-increment,  $\dot{\bar{\epsilon}}$  a scalar measure of the current strain rate, and  $\Delta \bar{\epsilon}$  the numerical admissible maximum strain increment.

According to Eq. (46), the value of  $\overline{\Delta t}$  is dependent on the current strain rate in the element.

As long as  $\Delta t < \overline{\Delta t}$ , the value of  $\overline{\Delta t}$  is forced to be equal to the value of  $\Delta t$ , which ensures the numerical stability and convergence from the viewpoint of the numerical integration of the constitutive equations. At high strain rate, the value of  $\Delta t$  could become lower than the value of  $\overline{\Delta t}$ . In this case, and for the element concerned, the sampling procedure is activated, using an optimised integration time increment such as  $\overline{\Delta t}_{\text{opt}} = \frac{\Delta t}{N}$ , where  $N = \text{Int}(\Delta t / \overline{\Delta t}) + 1$ .

The optimised integration time step is determined as follows:

$$\overline{\Delta t}_{\text{opt}} = \frac{\Delta t}{N} \quad \text{with} \quad \begin{cases} N = 1 & \text{if } \Delta t \leq \overline{\Delta t}, \\ N = \text{Int}\left(\frac{\Delta t}{\overline{\Delta t}}\right) + 1 & \text{if } \Delta t \geq \overline{\Delta t}. \end{cases} \quad (48)$$

This procedure involves a sub-loop for the concerned elements only. Considering the great number of elements, this last point is very important with regards to the calculation and (storage and dynamic) memory costs.

### 3.1. Analysed boundary value problem

Laboratory experiments able to generate loading conditions for adiabatic shearing are mainly:

- the dynamic torsion test employing a split Kolsky bar device (see for e.g. [12]);
- the dynamic plugging test employing a split Hopkinson pressure bar device (see for e.g. [35]);
- the dynamic double shearing test employing a direct Hopkinson bar device (see for e.g. [36]);
- the dynamic shearing of a HSS employing a split Hopkinson bar device (see for e.g. [37]);
- the Taylor test on cylinder(s) (see for e.g. [38]),...

We are here interested in the analysis of the particular HSS dynamic shearing test, called also ‘hydrodynamic hat test’ by COUQUE [39], (see Fig. 10a). This experiment performed in GIAT Industries laboratory consists in submitting a structure, whose geometry is close to top hat one, to a finite stress wave. The transient loading is generated by the direct impact of a striker bar onto the (A) side of the HSS, while the (B) side is in contact with the output bar. The HSS geometry (see Fig. 10b) has been designed and optimised (see [39]) in order to favour localisation of deformation in a well-defined area in which the pressure remains quasi constant and uniform. The objective of the test is to study the (relative) susceptibility of various metallic materials to ASB.

Loading conditions are expressed in terms of duration and load intensity which are controlled, respectively, by the striker length  $L_{\text{striker}}$  and the initial velocity  $V_{\text{striker}}$  of the striker. It can be

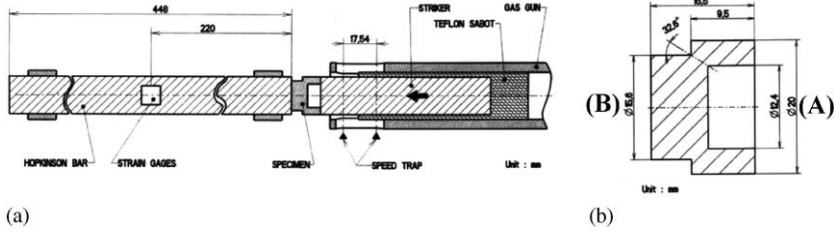


Fig. 10. HSS dynamic shearing test device (GIAT Industries): (a) HSS dynamic shearing test device; (b) HSS geometry.

easily shown that the longer is the loading duration, the larger is the strain, and that the higher is the loading intensity, the higher is the strain rate.

Let define the loading (nominal) period  $T$  as

$$T = \frac{2L}{c} \Big|_{\text{striker}}, \quad (49)$$

$$c_{\text{striker}} = \sqrt{\frac{E}{\rho_0}} \Big|_{\text{striker}}. \quad (50)$$

Because of the difference of mechanical impedance  $Z = \rho_0 c S$ , where  $S$  is the area, between the high strength steel HSS and the tungsten alloy bars, the HSS is submitted to several nominal loadings (at period  $T$ ) with decreasing magnitudes.

One of the aims of the present work consists in showing efficiency of the advanced constitutive model accounting for anisotropic deterioration induced dynamic degradation in order to estimate numerically integrity of a complex structure whose material is susceptible to ASB.

### 3.2. Numerical issues

Thanks to the modelling scale we use, neither particular mesh refining in any zone, nor the a priori knowledge of location and direction of adiabatic shear bands, is necessary.

In the following, the numerically simulated ASB-induced degradation of the HSS is analysed. Considering the experimental device symmetry, a quarter of the structure (as well as that of the striker and the output bars) has been discretised as shown in Fig. 11 employing elements with linear interpolation function and with a single integration point. Appropriate boundary conditions have been applied, including the initial velocity of the striker bar.

Predictive capacities of the numerical version of the model have been evaluated employing the set of material constants assembled in Table 4.

In the present model considering a RVE length scale greater than the band width, a distinction must be done between the adiabatic shear band itself and the degraded finite element (numerical RVE) supposed to contain the band. In numerical simulation, the term ‘deterioration band’ is actually a contraction of the expression ‘ASB -induced finite element deterioration band’. As long as a single finite element is affected, this term is abusive in the sense that the band is included in the finite element—there is no ‘true’ band but only a degraded finite element. But when the

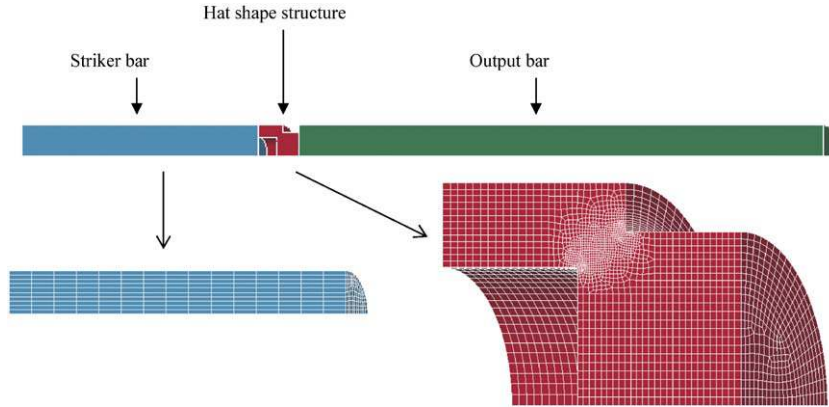


Fig. 11. Spatial discretisation of the HSS dynamic shearing test device.

Table 4  
Material constants for numerical simulation

Steel HSS TEVPVD model	Tungsten alloy bars Elastic model
$\rho_0 = 7800 \text{ kg/m}^3$	$\rho_0 = 17\,600 \text{ kg/m}^3$
$C = 420 \text{ J/kg K}$	
$E = 200\,000 \text{ MPa}$	$E = 320\,000 \text{ MPa}$
$\nu = 0.33$	$\nu = 0.3$
$\alpha = 1.e - 6 \text{ K}^{-1}$	
$R_i = 920 \text{ MPa}$	
$R_\infty = 400 \text{ MPa}$	
$k = 10$	
$\gamma = 1.1e - 3 \text{ }^\circ\text{C}^{-1}$	
$Y = 60 \text{ MPa s}^{1/n}$	
$n = 6$	
$a = 0 \text{ MPa}$	
$b = 15\,000 \text{ MPa}$	
$d_1 = 0.05$	
$d_2 = 0.05$	
$N = 2$	
$\eta_2 = 0.12 \text{ MPa}^{-2}$	
$Z = 19 \text{ MPa s}^{1/m}$	
$m = 2$	

degradation covers several finite elements, the notion of deterioration band (band of deteriorated finite elements) becomes appropriate. In this configuration, the deterioration band tip is the end of the shear zone formed by several degraded finite elements.

### 3.2.1. ASB-induced deterioration process

Various 3D numerical simulations have been performed. Depending on the impact velocity and on the loading duration, deterioration bands propagate or arrest inside the HSS.

Fig. 13a–d show four particular deterioration maps in the structure under the particular shock conditions (fairly intense loading) characterised by the couple ( $L_{\text{striker}} = 90 \text{ mm}$ ;  $V_{\text{striker}} = 30 \text{ m/s}$ ). They are to be analysed together with Fig. 14 that shows the evolution of the mean velocity for each deterioration branch tip, each one initiating from a corner (striker bar side and output bar side, respectively) of the HSS.

The mean orientation of the normal to the band plane—concerning the elements located in the (2,3) plane—is given by the angles  $\theta = 88^\circ$  and  $\phi = -30^\circ$  (see Fig. 12).

From the numerical viewpoint, HSS degradation happens thus in four stages (see Figs. 13–14):

- stage 1: ‘deterioration’ initiation in elements located near the HSS corners;
- stage 2: ‘deterioration’ band propagation at a quasi constant velocity (quasi steady propagation);
- stage 3: ‘deterioration’ band acceleration i.e. unsteady propagation before their junction;
- stage 4: deformation concentration in a single macro deterioration band resulting from the junction of two micro ‘deterioration’ bands.

These stages point out the progressivity in the ASB-induced degradation. This is in accordance with the experimental data available [12,40] and some analyses (see for e.g. [41]) which indicate gradual progression in bands development and propagation before final failure. The latter is neither immediate (after bands incipience) nor brutal. ASB preserve cohesion of matter for some lapse of time and assure reduced load transmission (they are not traction free entities).

During the 2nd stage (quasi-steady propagation), the value of the ‘deterioration’ band tip velocity is varying between 100 and 200 m/s. This value can reach 500 m/s during the 3rd stage (unsteady propagation).

In the configuration presented, these velocities which are greater than impact velocity remain much lower than the elastic shear wave celerity (for the material at stake), whose value is close to 3100 m/s.

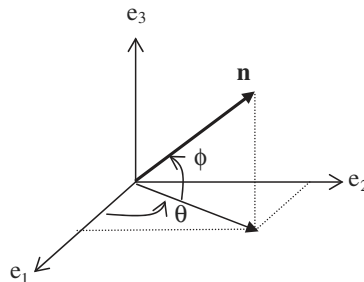


Fig. 12. Band orientation angles.

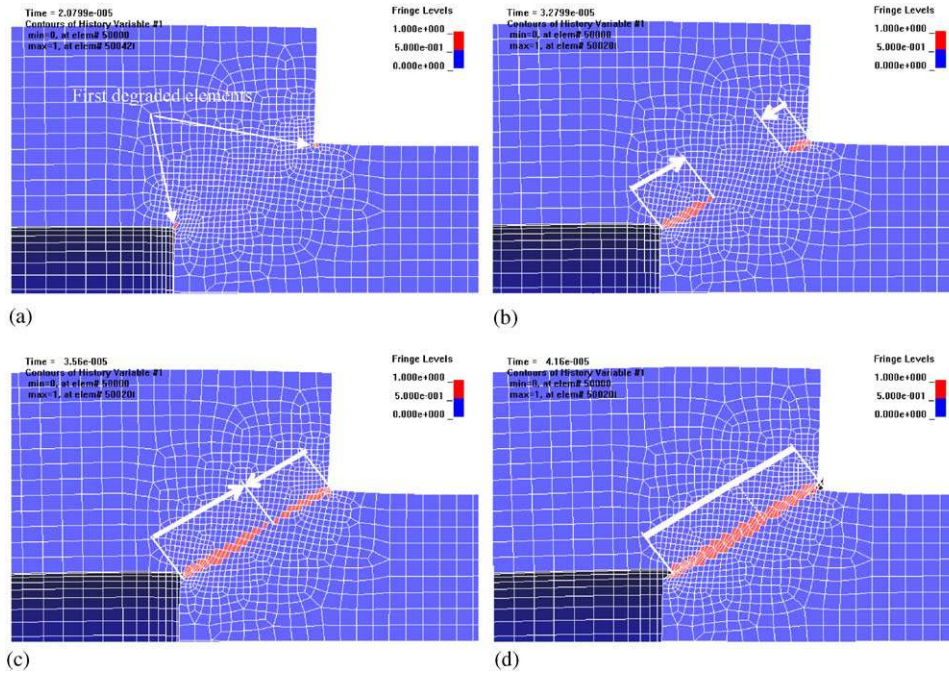


Fig. 13. Deterioration maps at different times and associated deterioration stages Affected elements  $\tilde{\mathbf{D}} \neq 0$  are depicted in red—Unaffected elements  $\tilde{\mathbf{D}} = 0$  are depicted in blue ( $L_{\text{striker}} = 90 \text{ mm} - V_{\text{striker}} = 30 \text{ m/s}$ ). (a) 1st stage: deterioration initiation; (b) 2nd stage: quasi steady propagation; (c) 3rd stage: unsteady propagation; (d) 4th stage: macro-localisation.

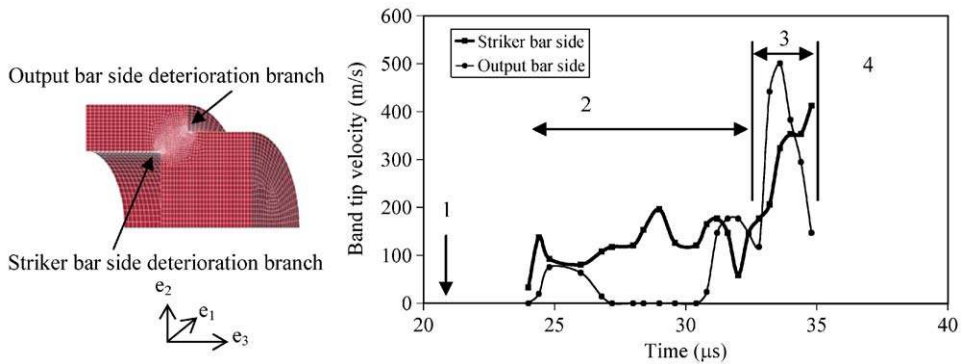


Fig. 14. Band tip velocity histories; time sequence of consecutive degradation stages ( $L_{\text{striker}} = 90 \text{ mm} - V_{\text{striker}} = 30 \text{ m/s}$ ).

### 3.2.2. Evolution of influent parameters during the deterioration process

Numerical histories of resolved shear stress, a measure of the ‘deterioration’ variable  $\tilde{\mathbf{D}}$ , ‘regular’ plastic strain, pressure and ‘regular’ temperature have been captured in various elements located in the deteriorated zone (see Fig. 15a).

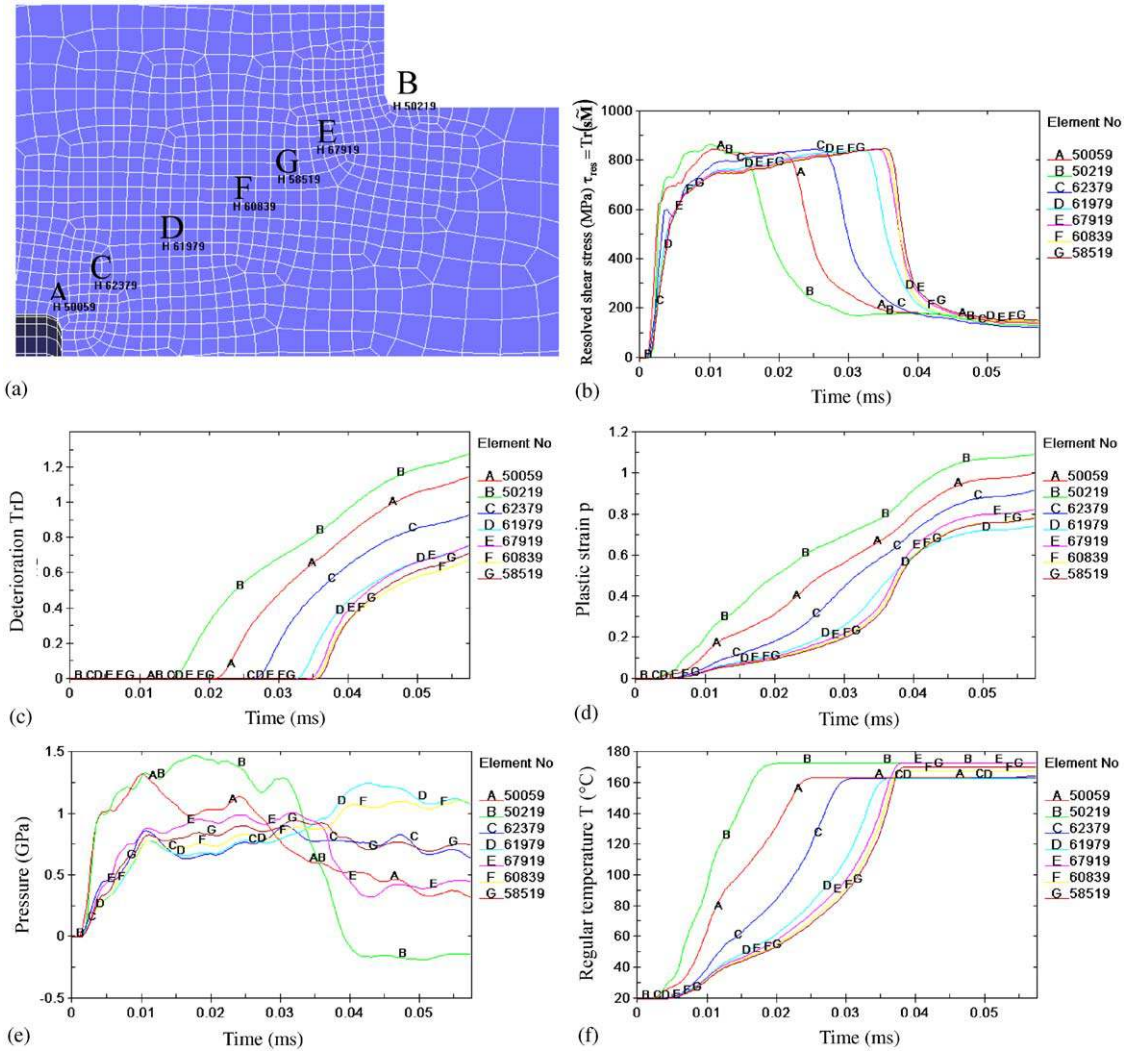


Fig. 15. Histories of influent parameters for the numerical simulation involving  $L_{striker} = 90$  mm and  $V_{striker} = 30$  m/s. (a) Numerical 'gauge' locations in the HSS; (b) resolved shear strain history; (c) deterioration history; (d) plastic strain history; (e) pressure history; (f) regular temperature history.

Fig. 15b shows clearly the consecutive stages of the material response during the dynamic loading: the hardening behaviour characterising the phase of predominant plasticity, and the drop in stress being induced by the deterioration process. The time to localisation onset is dependent on the element location—the distance to the stress concentrator at the origin of the deterioration incipience. This figure must of course be linked to the deterioration histories drawn in Fig. 15c.

It is to be noted that the interval of values taken by 'deterioration' tensor components is not normalised here to be, e.g. [0,1]. This is why the upper bound of  $Tr\tilde{\mathbf{D}}$  surpasses unity as well, see also [13].

Fig. 15d shows that the dissipative mechanism of ‘regular’ plasticity keeps on running during the deterioration process. At an advanced stage of deterioration, the band-induced deterioration becomes however predominant.

Fig. 15e points out the effect of stress concentration. For elements located at a distance far enough from the HSS corners, pressure can be considered as constant and uniform in the shear zone before the deterioration process (see also [39]).

From Fig. 15f, numerical evaluation of the temperature at the onset of ASB-induced deterioration is close to 150°C. ‘Regular’ temperature keeps on increasing until reaching a maximal value close to 170°C. Because of adiabaticity hypothesis, ‘regular’ temperature cannot decrease—as it would be the case if thermal transfer were accounted for. ‘Singular’ temperature (the temperature in the ASB) does rise significantly and its value can tend to the melting point, as it is described in the present approach through the increase in the deterioration intensity (see Fig. 15c). The maximum value  $d = 1.3$  (Fig. 15c) corresponds approximately to the singular temperature of 810 K (see [13] for further details).

Numerical histories of velocity and strain rate have been captured in various elements located far from the degraded zone, near the degraded zone and inside the degraded zone (see Fig. 16a).

Far from the degraded zone (elements A and B in Fig. 16a), after the initial peak the mean velocity (see Fig. 16b) is close to 8 m/s and the strain rate (see Fig. 16c) is lower than  $10^{+3} \text{ s}^{-1}$ .

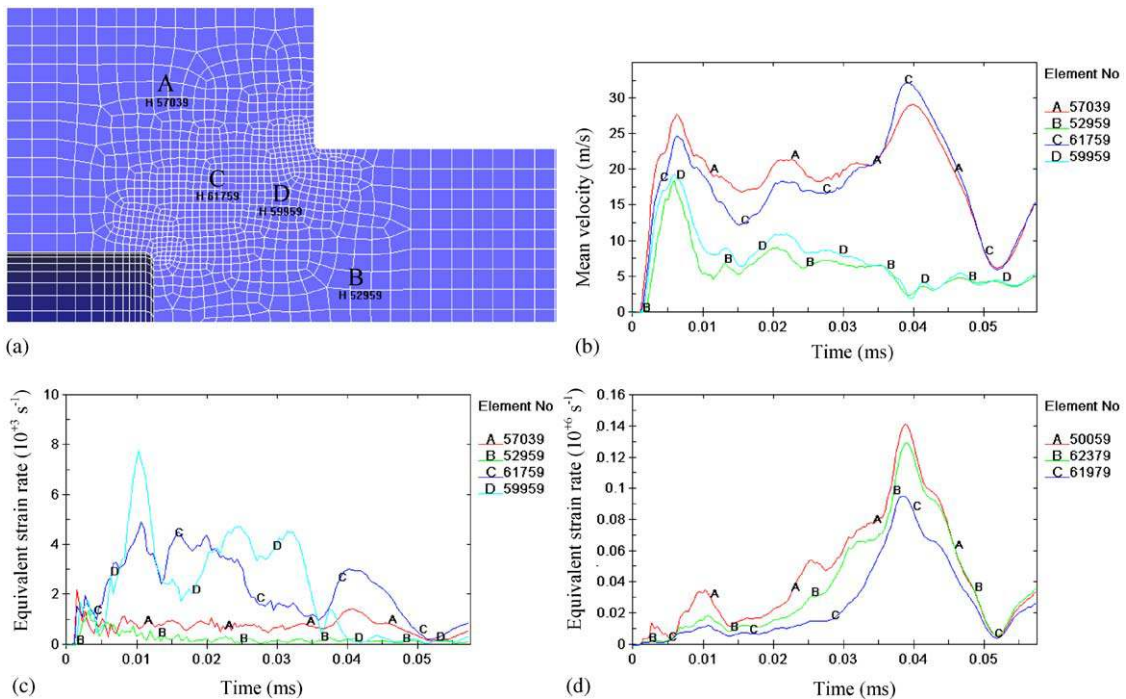


Fig. 16. Histories of velocities and strain rates for the numerical simulation involving  $L_{\text{striker}} = 90 \text{ mm}$  and  $V_{\text{striker}} = 30 \text{ m/s}$ . (a) Numerical ‘gage’ locations in the HSS; (b) mean velocity history (Locations A, B, C, D correspond to Fig. 12a); (c) equivalent strain rate history (outside the degraded zone) (Locations A, B, C, D correspond to Fig. 12a); (d) equivalent strain rate history (inside the degraded zone) (Locations A, B, C correspond to Fig. 11a).

Near the degraded zone (elements C and D in Fig. 16a), after the initial peak the mean velocity (see Fig. 16b) is close to 20 m/s, reaching 30 m/s before the unloading at  $42 \mu\text{s}$ , and the strain rate (see Fig. 16c) is close to  $4 \times 10^{+3} \text{ s}^{-1}$ .

Inside the degraded zone (elements A, B and C in Fig. 11a), the maximum strain rate (see Fig. 16d) is greater than  $10^{+5} \text{ s}^{-1}$ .

This rise in the strain rate inside the ‘degraded’ zone shows clearly the localised character of bands induced deterioration.

### 3.2.3. Interest in accounting for ASB-induced deterioration

Consider now the influence of the HSS material behaviour for the same loading case. Pictures in Fig. 17a and b show comparative deformation patterns of the HSS for a given time. The HSS is, respectively, composed of:

- material subject to thermal softening and ASB-induced degradation;
- material subject to thermal softening only.

In the first configuration (Fig. 17a), macro-localisation is evident, while in the second one (Fig. 17b), it is not (yet). From the numerical viewpoint, according to the present model, thermal softening itself could lead to a form of smooth stress weakening without significant drop of stress. The bands-induced deterioration, which includes the effect of ‘singular’ temperature  $T^*$  through the value of the density  $d(T^*, \dots)$ , see Section 1, coupled with ‘regular’ heat effect, produced realistic stress drop (see Fig. 15b). In such a way, neglecting the ASB-induced degradation would be too optimistic with regards to the prediction of the HSS integrity under dynamic loading.

### 3.2.4. Mesh size dependence

Numerical simulation of boundary value problems in presence of material instabilities, i.e. softening behaviour, leads necessarily to questions about the mesh dependence of the numerical results. The constitutive model proposed involves double viscosity effects concerning inelastic

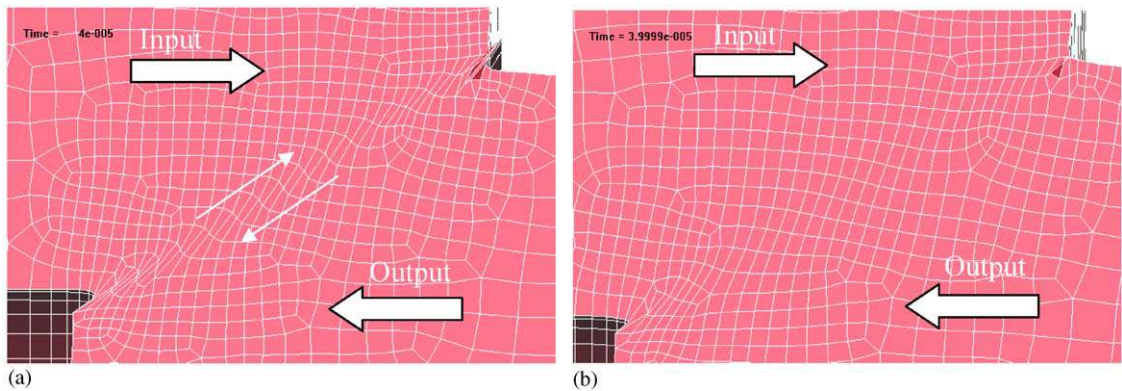


Fig. 17. Deformation state at  $40 \mu\text{s}$  ( $L_{\text{striker}} = 90 \text{ mm}$  –  $V_{\text{striker}} = 30 \text{ m/s}$ ): (a) Material subject to thermal softening and ASB-induced degradation; (b) material subject to thermal softening only.

deformation as well as the bands-induced deterioration evolution; these viscosity effects constitute obviously a regularising factor, see [7,33]. They do not eliminate completely mesh-size effects.

In order to estimate qualitatively some residual mesh size dependence, several configurations have been tested using different mesh densities (designated here ‘fine’, ‘medium’ and ‘coarse’) in the intense shear zone, as shown in Fig. 18. The mean area  $A$  of the elements located inside the intense shear zone is also given.

In Fig. 19, the degraded area—obtained by counting the number of degraded elements—is drawn versus time. The maximum degraded area corresponds to the junction of both degraded branch tips.

The evolution of the degraded areas for the three types of meshing seems very similar in the first steps of the HSS deterioration, but the maximum degraded area is actually different between the fine meshing configuration and the medium and coarse configurations. In the former case, the degraded band width is equal to the element size, while for the medium and coarse discretisations the degraded band width can cover two elements—the disorientation of the elements for medium-coarse meshings constricts the degraded band propagation. However, preserving the physics of the ASB phenomenon in the framework of the present model (viz. super dislocation concept) implies employing an element size greater than the ASB width, excluding thus the use of too fine meshing. Comparing the medium and coarse configurations, one can conclude a relatively weak sensitivity of the numerical results to the mesh size.

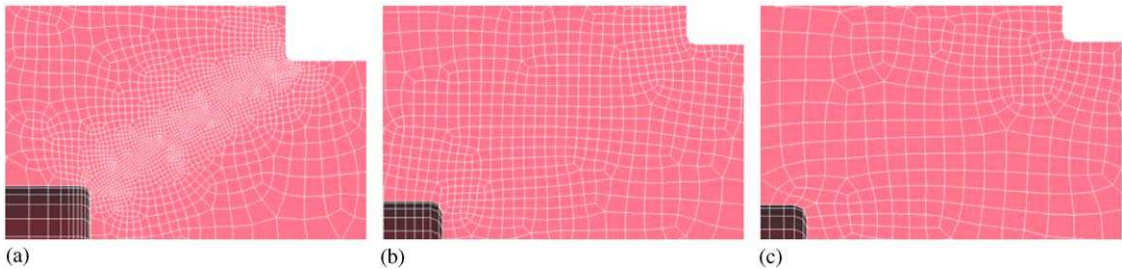


Fig. 18. Mesh sizes ( $L_{\text{striker}} = 90 \text{ mm} - V_{\text{striker}} = 30 \text{ m/s}$ ). (a) Fine meshing (high density— $A = 2,14 \times 10^{-3} \text{ mm}^2$ ); (b) medium meshing (medium density— $A = 10^{-2} \text{ mm}^2$ ); (c) coarse meshing (low density— $A = 2,2 \times 10^{-2} \text{ mm}^2$ ).

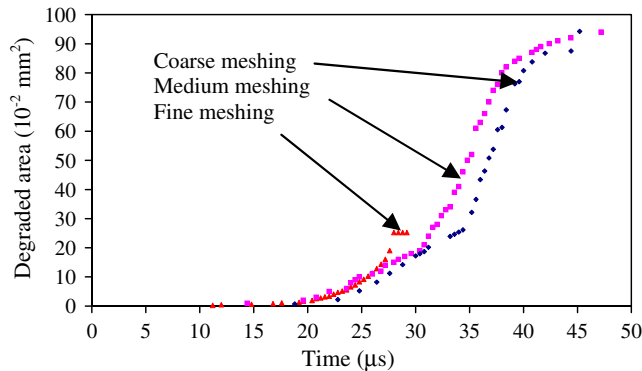


Fig. 19. Degraded area history.

#### 4. Numerical predictions vs. experimental observations

As stated in the introduction of this paper, the aim of the actual modelling is to incorporate the ASB induced anisotropic degradation in the evaluation of the structural integrity under dynamic loading, as for example encountered in the problems of dynamic penetration and perforation. The challenge of the 3D modelling developed in Section 2 is clearly turned towards the description of the material response not only during the stage of locally homogeneous (and weakly inhomogeneous) deformation but also during the stage of ASB-induced post (strong) localisation. This section is devoted to the evaluation of the predictive capacities of the model in a particular test configuration.

In laboratory experiments employed for studying the ASB phenomenon, the major difficulty consists in putting together the boundary conditions favourable for initiating and developing ASB, the control of the location and of the propagation of the ASB, and the measurement tools allowing for extrapolating reliable enough (in time and space) information relative to the band microstructure, temperature, deformation and/or resistance. In spite of the great number of measurement means available today (strain gauges, thermal sensors, high-speed cameras, ...), it is not yet possible to get all this information together. For this reason, numerical simulation constitutes a necessary complementary investigation tool.

We are here interested in the use of the HSS dynamic shearing test for the study of the (relative) susceptibility of various metallic materials to ASB. As stated before, the loading conditions are defined as loading intensity controlled by the striker initial velocity and loading duration controlled by the striker length. The material of the study is a hard structural steel (30NiCrMo-6-6 with appropriate thermo-mechanical treatment).

In parallel, 3D full-scale numerical simulations have been performed using the finite element code LS-DYNA with the TEVPVD constitutive model as user material (Table 3). Initial and boundary conditions have been respected regarding the experimental conditions. Initiation and propagation of ASB-induced deterioration bands is controlled by the critical value of the energy release rate  $k_{inc}$  (deterioration conjugate force) which is obtained from a criterion relating the current resolved shear stress to material parameters (see Section 2.2). In the following sub sections, two configurations involving, respectively, partially propagated ASB/deterioration bands and totally propagated ASB/deterioration bands are considered; post-mortem optical photographs and deterioration maps are compared as well as the experimental/numerical load transmitted to the output bar.

##### 4.1. Configuration involving partially propagated ASB/deterioration bands

This configuration is characterised by a long loading duration ( $L_{striker} = 200$  mm) and a low loading intensity ( $V_{striker} = 17.8$  m/s).

The reconstituted post-mortem optical photograph [42] in Fig. 20 reveals the presence of a truncated cone shape adiabatic shear band. The propagation of the adiabatic shear band tip has been arrested inside the intense shear zone.

Numerical deterioration map in Fig. 21 for  $t = 150 \mu s$  ( $t = 1.5 T$ ) reveals the presence of partially propagated deterioration branches. The deterioration branch initiated near the striker bar side corner has much more propagated.

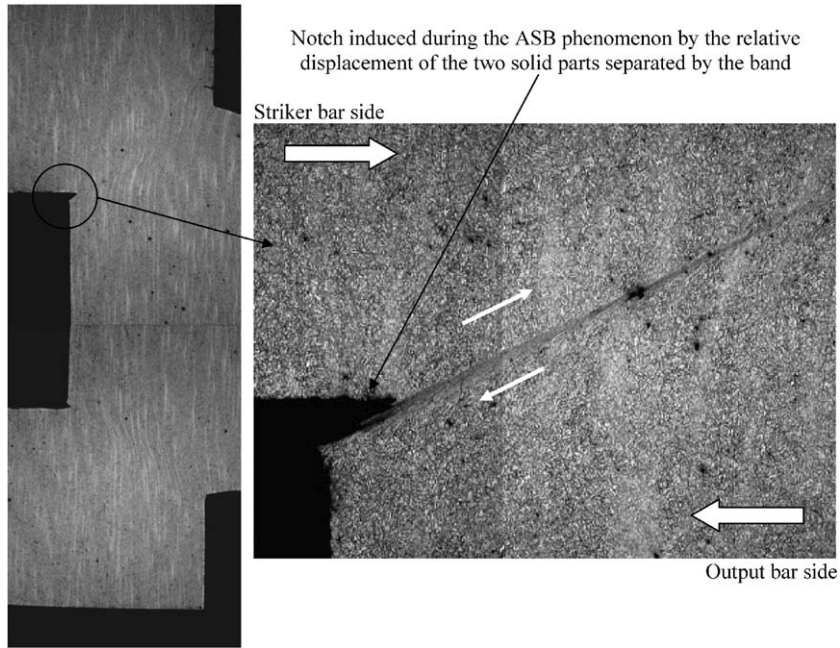


Fig. 20. Experimental observation; loading configuration:  $L_{\text{striker}} = 200 \text{ mm}$ ,  $V_{\text{striker}} = 17.8 \text{ m/s}$  ( $T = 93.8 \mu\text{s}$ ).

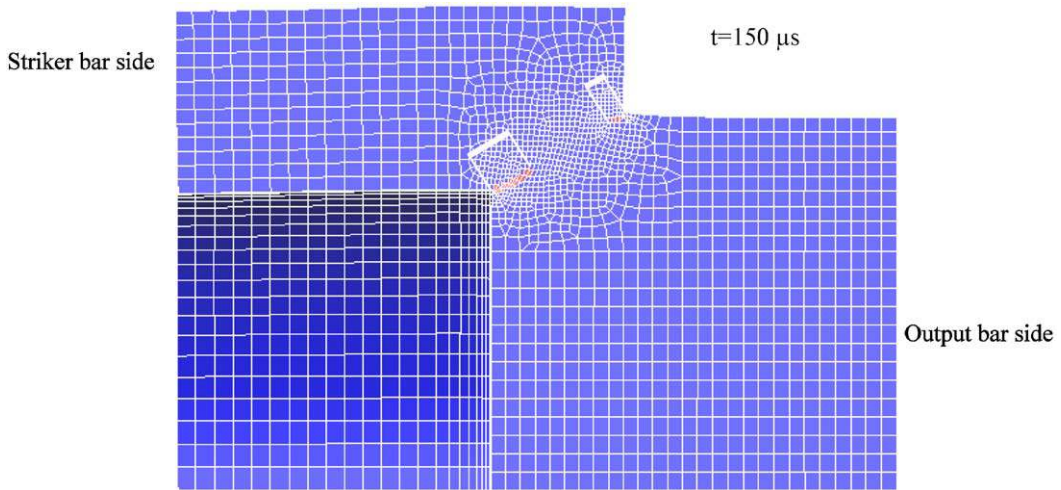


Fig. 21. Numerical prediction (medium meshing); loading configuration:  $L_{\text{striker}} = 200 \text{ mm}$ ,  $V_{\text{striker}} = 17.8 \text{ m/s}$  ( $T = 93.8 \mu\text{s}$ ).

To avoid a possible confusion between observed adiabatic shear band and predicted numerical deterioration band, it must be recalled here that, according to our scale of modelling, the ASB is included in the deterioration band. This implies that the numerical deterioration band width is

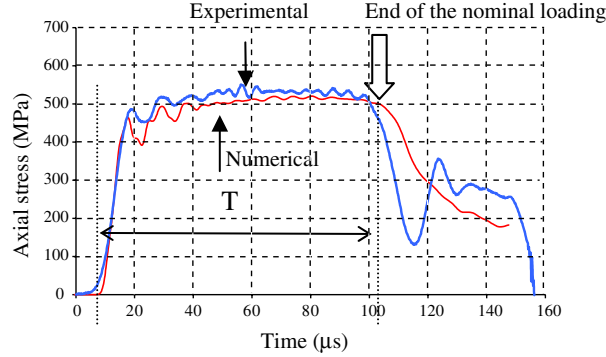


Fig. 22. Comparison theory vs. experiment for axial stress transmitted to the output bar; loading configuration:  $L_{\text{striker}} = 200 \text{ mm}$ ,  $V_{\text{striker}} = 17.8 \text{ m/s}$  ( $T = 93.8 \mu\text{s}$ ).

greater than the ASB width. The deterioration band can thus be considered as the zone the more affected by the presence of the band.

The comparison of the numerical deterioration map (Fig. 21) with the post-mortem macrograph (Fig. 20) is satisfying from the qualitative viewpoint.

Experimental [43] and numerically simulated loading curves, expressed in terms of axial stress, transmitted to the output bar, are superposed in Fig. 22. During the nominal loading duration ( $0 < t \leq T$ ), the experimentally measured load transmitted to the output bar is close to the one predicted numerically. There is a weak difference in the load evolution during the unloading ( $t > T$ ) but the interferences between incident and reflected waves in the output bar (due to significant length of the striker bar) limit the interpretation of both experimental and numerical values at this stage.

Finally, a good global agreement between experimental and numerical curves is to be noticed.

#### 4.2. Configuration involving totally propagated ASB/deterioration bands

This configuration is characterised by a short loading duration ( $L_{\text{striker}} = 40 \text{ mm}$ ) and a high loading intensity ( $V_{\text{striker}} = 35.6 \text{ m/s}$ ).

The post-mortem optical photograph [42] in Fig. 23 reveals the presence of a crossing crack at the HSS ‘upper’ side and the presence of a crossing adiabatic shear band with a partial crack at the HSS ‘lower’ side. This loss of axial symmetry in the failure mode, not observed in the previous case (see Fig. 20), is probably the consequence of the existence of many ASB-deterioration nucleation sites which are not activated at the same time. The formation of the band-plane (and later of the plane crack) is actually the advanced stage of more or less diffuse evolution of several joint micro band surfaces (an analogy can be drawn with the coalescence of cavities in the case of ductile fracture). This diffuse process involving possible ‘obscured regions’, i.e. relaxed zones in the neighbourhood of ASB, see [44] for some analogy with crack-induced ‘relaxed’ zones, is probably favoured by possible defects in the coaxiality of the experimental device in the context of strong stress concentrations.

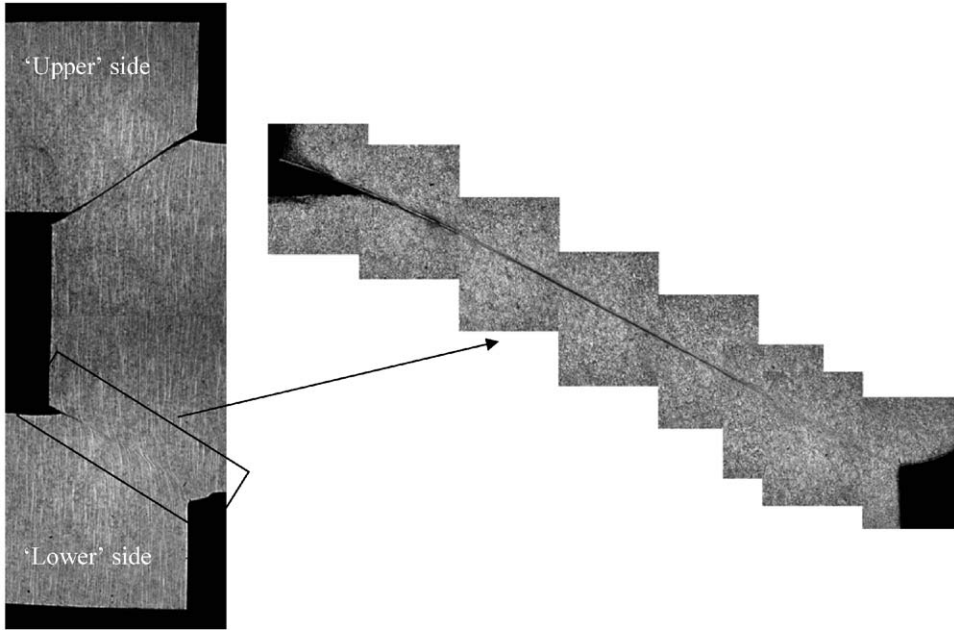


Fig. 23. Experimental observation; loading configuration:  $L_{\text{striker}} = 40 \text{ mm}$ ,  $V_{\text{striker}} = 35.6 \text{ m/s}$  ( $T = 18.7 \mu\text{s}$ ).

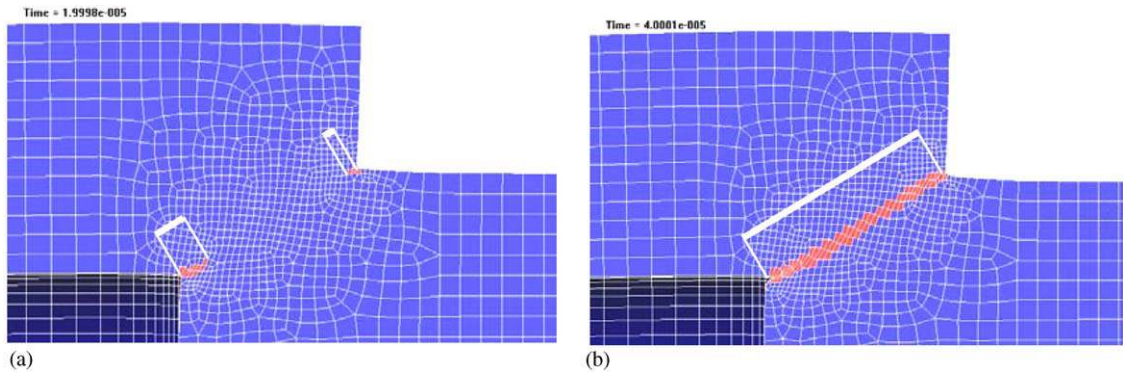


Fig. 24. Numerical deterioration maps: (a)  $t \approx T$ ; (b)  $t \approx 2T$  (Affected elements  $\tilde{\mathbf{D}} \neq 0$  are depicted in red—Unaffected elements  $\tilde{\mathbf{D}} = 0$  are depicted in blue); loading configuration:  $L_{\text{striker}} = 40 \text{ mm}$ ,  $V_{\text{striker}} = 35.6 \text{ m/s}$  ( $T = 18.7 \mu\text{s}$ ).

Numerical deterioration map in Fig. 24b for  $t = 2T$  reveals the presence of a crossing deterioration band. The introduction of genuine decohesion threshold in the TEVPVD constitutive model is yet to be done. On the other hand the transition to macroscopic fracture being not trivial, it deserves prospective reflection from the mechanical and numerical viewpoints. Numerical simulations presented here do not predict any macro-crack initiation and propagation.

Considering Fig. 24a and b, the junction of both deterioration branches (each one initiated from each HSS corner) occurs during the second nominal loading ( $T < t = 2T$ ). Numerical simulation turns out to be effective to provide this information.

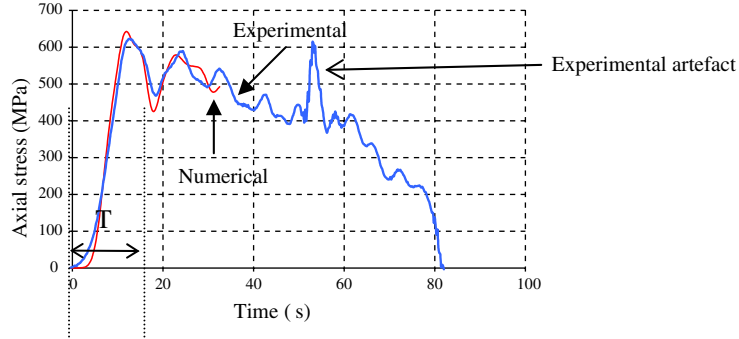


Fig. 25. Comparison theory vs. experiment for axial stress transmitted to the output bar; loading configuration:  $L_{\text{striker}} = 40 \text{ mm}$ ;  $V_{\text{striker}} = 35.6 \text{ m/s}$  ( $T = 18.7 \mu\text{s}$ ).

Considering this severe test configuration, numerical simulation tends to reproduce well the experimental observations.

According to Fig. 25, the HSS is submitted to several loadings with the same period  $T$  but with decreasing magnitudes—this is the direct consequence of the difference in mechanical impedance between the bars and the HSS. The three consecutive loadings ( $0 < t \leq 3T$ ) are however high enough to maintain the evolution of the ASB process until crack growth for  $t > 3T$ .

Once again, experimental observations [43] and numerical results are in good agreement.

#### 4.3. Summary

The experimental and numerical results shown above are a part of a series of numerous configurations tested. They show good predictive capacity of the model developed in Section 2. They show, furthermore, the necessity to account for the history dependent ASB-induced degradation for the prediction of the loss of structural integrity under dynamic loading. The description of the ASB deterioration effects solely in the terms of thermal softening—with a mesh size greater than the band width—and/or brutal failure (while adiabatic shearing preserves matter cohesion keeping on transmitting a part of loading) is not fully satisfactory and leads to rather coarse assessments of non-linear response of impacted structures. Moreover, in more complex boundary value problems, considering ASB-induced deterioration as isotropic can also be a source of oversimplification, notably as concerns band trajectory.

Depending on the loading conditions, adiabatic shear bands initiate or not, propagate or arrest inside the HSS, showing thus complex (non-linear) history effects. Intense shocks lead in most cases to macroscopic cracking and failure. The latter is to be dealt with to complete the present non-linear model.

### 5. Concluding remarks and perspectives

Based on irreversible thermodynamics, the three-dimensional finite deformation constitutive model has been formulated including anisotropic deterioration (deterioration-like) effects

related to ASB incipience and growth. It is intended to be applied to evaluate dynamic degradation, i.e. loss of integrity for impacted structures where ASB is preponderant failure mechanism.

The model is rate sensitive and includes ASB deterioration-induced anisotropy as well as obvious strain hardening vs. thermal softening competition. It is supposed to respond to growing need of genuine non-linear modelling able to reproduce behaviour of a wide class of metallic materials under high strain rate loading. The post-localisation behaviour (in the presence of ASB) is being fairly described while double viscous regularisation coming from ‘regular’ plasticity evolution as well as from ASB-induced viscous deterioration assures the stable integration algorithm and reduces strongly the mesh sensitivity effects.

The model has been implemented as user material in the finite element code LS-DYNA. Initiation, orientation and propagation of deterioration bands are supposed to be controlled by the constitutive model presented involving an auxiliary condition relating the resolved shear stress, the isotropic hardening conjugate force, the strain rate-induced overstress, the plastic hardening and the thermal softening. Consequently critical values of temperature and deformation at the occurrence of the ASB-induced deterioration process are not arbitrary imposed but intimately linked to the loading path under consideration in the general three-dimensional context. The quantitative mesh dependence study confirms a significant attenuation effect of double viscosity-induced pseudo-regularisation, i.e. globally weak mesh-sensitivity in the presence of deterioration bands. Numerical simulations considering the dynamic shearing for the hat shape structure have been performed showing a good accordance of the model predictions with the corresponding experimental data. This comparison allows inferring satisfactory predictive capacities of the constitutive model proposed involving 3D character and anisotropy of the ASB mechanism. Transition to macroscopic failure constitutes clearly the next step in the modelling of ASB-induced effects.

## References

- [1] Zener C, Hollomon JH. Effect of strain rate upon plastic flow steel. *J Appl Phys* 1944;15:22–32.
- [2] Recht RF. Catastrophic thermoplastic shear. *J Appl Mech (Trans ASME)* 1964;31E:189–93.
- [3] Bai YL, Dodd B. *Adiabatic shear localisation*. Oxford: Pergamon Press; 1992.
- [4] Wright TW. *The physics and mathematics of adiabatic shear bands*, Series: Cambridge monographs on mechanics. Cambridge University Press, 2002.
- [5] Woodward RL. Material failure at high strain rates. In: Zukas JA, editor. *High-velocity impact dynamics*. New York: Wiley; 1990. p. 65–125.
- [6] Pecherski RB. Macroscopic effects of micro-shear banding in plasticity of metals. *Acta Mech* 1998;131:203–24.
- [7] Perzyna P. Influence of anisotropic effects on the micro-damage process in dissipative solids. In: J. P. Bohler, (editor). *Yielding, damage, and failure of anisotropic solids*, Mechanical Engineering Publisher, 1990. p. 483–507.
- [8] Lubarda VA. An analysis of large-strain damage elastoplasticity. *Int J Solids Struct* 1994;31(21):2951–64.
- [9] Mandel J. Equations constitutives et directeurs dans les milieux plastiques et viscoplastiques. *Int J Solids Struct* 1973;9:725–40.
- [10] Sidoroff F, Dogui A. Some issues about anisotropic elastic–plastic models at finite strain. *Int J Solids Struct* 2001;38:9569–78.
- [11] Mercier S. *Etude de la formation et de la propagation d’une bande de cisaillement adiabatique*. PhD thesis, Université de Metz, 1997.

- [12] Marchand A, Duffy J. An experimental study of the formation process of adiabatic shear bands in a structural steel. *J Mech Phys Solids* 1988;36(3):251–83.
- [13] Longere P, Dragon A, Trumel H, De Ressaéguier T, Deprince X, Petitpas E. Modelling adiabatic shear banding via damage mechanics approach. *Arch Mech* 2003;55:3–38.
- [14] Dragon A, Halm D. Damage mechanics—Some modelling challenges. AMAS lecture notes series, 9, Warsaw; Centre of Excellence for Advanced Materials and Structures (AMAS): 2004.
- [15] Ekh M, Runesson K. Modeling and numerical issues in hyperelasto-plasticity with anisotropy. *Int J Solids Struct* 2001;8:9461–78.
- [16] Mandel J. Relations de comportement pour un solide élastoplastique anisotrope en transformation finie. In: *Colloques internationaux du CNRS, Vol. 319. Comportement plastique des solides anisotropes*, 1981. p. 197–210.
- [17] Dafalias YF. A missing link in the macroscopic constitutive formulation of large plastic deformations. In: Sawczuk A, Bianchi G, editors. *Plasticity today*. Amsterdam: Elsevier; 1983.
- [18] Boehler JP. Lois de comportement anisotropes des milieux continus. *J Méc* 1978;17:153–90.
- [19] Dragon A, Halm D, Désoyer T. Anisotropic damage in quasi-brittle solids: modelling, computational issues and applications. *Comput Methods Appl Mech Eng* 2000;183:331–52.
- [20] Taylor GI, Quinney MA. The latent energy remaining in a metal after cold working. *Proc Royal Soc A* 1934;413.
- [21] Baltov A, Sawczuk A. A rule of anisotropic hardening. *Acta Mech* 1965;1:1–81.
- [22] Shrivastava BP, Mroz Z, Dubey RN. Yield criterion and the hardening rule for a plastic solid. *ZAMM* 1973;53:625–33.
- [23] Maugin GA. *The thermomechanics of nonlinear irreversible behaviours. An introduction*. Singapore: World Scientific; 1999.
- [24] Perzyna P. Fundamental problems in viscoplasticity. *Adv Appl Mech* 1966;9:243–377.
- [25] Bai YL. Thermo-plastic instability in simple shear. *J Mech Phys Solids* 1982;30(4):195–207.
- [26] Clifton RJ, Duffy J, Hartley KA, Shawki TG. On critical conditions for shear band formation at high strain rates. *Scripta Met* 1984;18:443–8.
- [27] Molinari A. Collective behavior and spacing of adiabatic shear bands. *J Mech Phys Solids* 1997;45(9):1551–75.
- [28] Johnson GR, Cook WH. A constitutive model and data for metals subjected to large strains, high strain rates and high temperatures. In: *Proceedings of the seventh international symposium on ballistics*, The Hague, The Netherlands, 1983. p. 541–7.
- [29] Zerilli FJ, Armstrong RW. Dislocation mechanics-based constitutive relations for material dynamics calculations. *J Appl Phys* 1987;61:1816–25.
- [30] Gailly B. *Etude du comportement dynamique et de la rupture de trois aciers à blindage*. PhD thesis, Ecole Nationale Supérieure des Mines de Paris, 1996.
- [31] Molinari A. Instabilité thermoviscoplastique en cisaillement simple. *J Méca Théor Appl* 1985;4:659–84.
- [32] Courant R, Friedrichs KO, Lewy H. On the partial difference equations of mathematical physics. *IBM J* 1967;11:215–34.
- [33] Dornowski W, Perzyna P. Localisation phenomena in thermo-viscoplastic flow processes under cyclic dynamic loadings. *Comput Assist Mech Engng Sc* 2000;7:117–60.
- [34] Kulkarni M, Belytschko T, Bayliss A. Stability and error analysis for time integrators applied to strain-softening materials. *Comput Methods Appl Mech Eng* 1995;124:335–63.
- [35] Mazeau C, Beylat L, Longere P, Louvigné PF. On the quantitative evaluation of adiabatic shear banding sensitivity of various titanium alloys. *J Phys* 1997;IV:429–34.
- [36] Klepaczko JR, Klosak M. Numerical study of the critical impact velocity in shear. *Eur J Mech A/Solids* 1999;18:93–113.
- [37] Beatty JH, Meyer LW, Meyers MA, Nemat-Nasser S. Formation of controlled adiabatic shear bands in AISI4340 high strength steel. In: Meyers MA, Murr LE, Staudhammer KP, editors. *Shock-wave and high-strain-rate phenomena in materials*. New York: Marcel Dekker; 1992. p. 645–56.
- [38] Holt WH, Mock W, Zerilli FJ, Clark JB. Experimental and computational study of the impact deformation of titanium Taylor cylinder specimens. *Mech Mat* 1994;17:195–201.
- [39] Couque H. A hydrodynamic hat specimen to investigate pressure and strain rate dependence on adiabatic shear band formation. *J Phys IV* 2003;110:423–8.

- [40] Xue Q, Meyers MA, Nesterenko VF. Self-organization of shear bands in titanium and Ti-6Al-4V alloy. *Acta Mat* 1996;50:575–96.
- [41] Mercier S, Molinari A. Steady-state shear band propagation under dynamic conditions. *J Mech Phys Solids* 1998;46(8):1463–95.
- [42] Lescure JM. GIAT Industries, Technical notes DSAM/DT/DRM no214b-170b-30b/02,2003.
- [43] Couque H. Essais chapeau hydrodynamique d'un acier. Technical note DSAM/DT/MCP/3050.13.03C, GIAT Industries, 2003.
- [44] Dénoual C, Hild F. Dynamic fragmentation of brittle solids: a multi-scale model. *Eur J Mech A* 2002;21:105–20.